Combustion and Flame 245 (2022) 112327

Contents lists available at ScienceDirect

Combustion and Flame

journal homepage: www.elsevier.com/locate/combustflame

Nanosecond pulsed plasma assisted combustion of ammonia-air mixtures: Effects on ignition delays and NO_x emission

Taaresh Sanjeev Taneja, Praise Noah Johnson, Suo Yang*

Department of Mechanical Engineering, University of Minnesota – Twin Cities, Minneapolis, MN 55455, USA

ARTICLE INFO

Article history:
Received 1 February 2022
Revised 5 August 2022
Accepted 6 August 2022

Keywords:
Plasma assisted combustion
Ammonia combustion
Vibrational excitation
Ignition delay
NO_x emission
Reaction pathway analysis

ABSTRACT

Computational investigation of plasma assisted combustion of ammonia-air mixtures in constant volume and constant pressure reactors are conducted, to determine the impact of operating conditions on ignition delays and NO_x emissions. Due to the lack of a chemical kinetic mechanism for plasma discharge of ammonia (NH_3)/air mixtures, a mechanism has been assembled in this work using well-validated plasma reactions of NH_3 with O_2 and N_2, alongside plasma kinetics of air from the literature. The impact of the reduced electric field (E/N), equivalence ratio, pressure, pulse frequency and the energy density on the ignition delays and NO/NO_2 emission is discussed. At lower E/N, vibrational-to-translational (VT) relaxation of the vibrational states of NH_3 and N_2 is observed to play a dominant role in the gas heating process on account of the higher vibrational energy contribution. The ignition event is observed to be faster for fuel-lean mixture ($\phi = 0.5$) compared to stoichiometric and fuel-rich ($\phi = 1.2$) conditions owing to the lower consumption of OH radicals through the reactivity-inhibiting reaction $NH_3 + OH \rightarrow NH_2 + H_2O$ between plasma pulses for leaner mixtures. Nevertheless, the fuel-lean mixture is observed to exhibit higher production of NO_x than stoichiometric and fuel-rich mixtures, resulting from plasma chemistry involving oxygen radical and electronic excited states of N_2. At the higher pressure of 3 atm, the pressure dependent recombination reaction $H + O_2 + M \rightarrow HO_2 + M$ is found to delay the ignition by limiting the reactive radicals compared to the corresponding 1 atm case. Higher rates of collisional quenching at higher pressures during the inter-pulse gaps resulted in lesser amount of electronically excited states of N_2 and O_2, which resulted in lower production of air-bound NO_x during the pulses. Pulse frequency and energy density per pulse are seen to exhibit an inversely proportional effect on the ignition delay times. Most importantly, a faster ignition and lower production of NO_x is observed in the case of plasma discharges compared to thermal energy deposition, owing to the enhanced production of OH radicals and the reforming of NH_3 to produce N_2 with plasma, respectively. Interesting roles of fuel-radicals such as NH_2 and NH in both producing and reducing NO at different instants have also been discussed.

1. Introduction

Increasing emphasis on the de-carbonization of energy production has led researchers to consider carbon free, renewable and green fuels such as hydrogen (H_2) and ammonia (NH_3). While H_2 suffers from the major challenges of production difficulties, transportation, and storage, NH_3 is plagued with challenges of low flame speeds causing unstable flames, high autoignition temperatures resulting in longer ignition delays, narrow flammability limits, and higher levels of NO_x emission [1]. Most of these effects get further pronounced in high-pressure systems such as gas turbines and internal combustion engines.

Different solutions to overcome these challenges of ammonia combustion have been proposed in the literature. Blending NH_3 with H_2 is one popular method which enhances the burning velocity of the mixture owing to the higher mass diffusivity of H_2. This was recently discussed in Wiseman et al. [2] where, for identical strain rates, an $NH_3/H_2/N_2$ blend was shown to have better resilience against blow-off as compared to a methane (CH_4)/air mixture even under highly sheared turbulence. This effect was attributed to the fast diffusion of H_2 in the spatially distributed preheat layers which enhanced the local heat release rates. An assessment of ideal blending percentage of H_2 in NH_3/H_2 fuel blends, overall equivalence ratio, and intake pressures in spark ignition engine conditions, was discussed in Lhuillier et al. [3]. Ideal blends provided benefits in terms of avoiding misfires, providing cyclic stability while maintaining maximum possible efficiency. Nevertheless, higher than optimal H_2 fractions resulted in

* Corresponding author.
E-mail address: suo-yang@umn.edu (S. Yang).

https://doi.org/10.1016/j.combustflame.2022.112327
0010-2180/

depleted efficiencies due to increased wall heat losses. Feasibility of using rich mixtures of a 70% NH_3 - 30% H_2 (in terms of mole fraction) blend under gas turbine conditions was discussed in Valera-Medina et al. [4]. Faster consumption of fuel species due to flame contraction under high inlet temperatures was observed, which represented improved combustion efficiencies. Reactions of unburned NH_3 with NO_x were shown to be responsible for reduction of overall NO_x emission due to the production of NH_x radicals. Nevertheless, this blend was still deemed significantly worse in terms of efficiency and NO_x emission, as compared to traditional fuels such as CH_4. Hayakawa et al. [5] reported lower NO formation for rich premixed NH_3/air mixtures ($\phi = 1.1$) compared to lean ($\phi = 0.7$) and stoichiometric mixtures. The decrease in NO in case of rich mixtures was attributed to the increased amounts of NH_3 radicals (NH_2, NH, and N), which react with NO, thereby depleting it. The study [5] also observed a reduction in NO at high pressures (about 0.3 MPa), due to the increased rates of $H + OH + M \rightarrow H_2O + M$ to preclude the formation of NO by faster consumption of H and OH radicals.

While research pursuits on NH_3/H_2 blended fuels seem to address some issues of traditional NH_3 combustion, producing H_2 still remains a challenge. Since NH_3 itself is a hydrogen carrier, research is being done on cracking of NH_3 to produce H_2. However, the major challenge with cracking of NH_3 to form H_2 is the requirement of a large surface area to volume ratio for catalyst based decomposition [6,7]. This makes scaling up of such reactors for on-board conversion of NH_3 to H_2 very difficult. Moreover, the decomposition rates of NH_3 on commonly used ruthenium surface reactors is quite sensitive to temperature as is explained in Klerke et al. [8]. Often, temperatures in excess of 600 K are required for these catalysts to be active in producing appreciable yields of H_2 [8]. Supplying heat to achieve this endothermic process poses major challenges in terms of system efficiency as well as physical construction to facilitate on-board H_2 production. In addition, a mechanism to separate H_2 from the equilibrium NH_3 stream is also required. The alternative option, thermal decomposition of NH_3, would require a lot of preheating, which again decreases the overall system efficiency.

In comparison, non-equilibrium plasma based igniters can easily be integrated into modern gas turbines and internal combustion (IC) engines, and can promote localized volumetric ignition kernel development by both thermal and chemical assistance. Moreover, these plasma based igniters can be actively controlled based on the mixture equivalence ratio, initial temperature and pressure, and other design and operating conditions of the combustion system. Various studies have focused on modeling the combustion and plasma kinetics of combustible gas mixtures. Faingold and Lefkowitz [9] developed a plasma kinetic mechanism for NH_3/O_2/He mixtures and studied the impact of pulse repetition frequency on building a radical pool at atmospheric pressure and temperatures ranging from 600 to 1500K. Similar studies aimed at exploring the effect of chemical pathways of radical production and consumption were found to be available for other fuels such as CH_4 [10,11], n-heptane [12] and dimethyl-ether (DME) [13]. Non-equilibrium plasma is known to facilitate unique chemical pathways for fuel pyrolysis, enhanced O radical generation, and ultra-fast heating that drives up the rates of several combustion reactions. These fundamental and technological advantages of non-equilibrium plasma could allow the direct combustion of pure or high concentration NH_3, as opposed to blending it with other fuels or decomposing it to form H_2.

Complementing the modeling front, Shioyoke et al. [14] explored the two-stage simulation methodology to investigate the enhancement of laminar burning velocity (LBV) of a premixed NH_3/air flame under non-equilibrium plasma discharges. Specifically, the plasma discharge is simulated in a perfectly stirred reactor (PSR), and the species concentrations and temperature of this reactor are served as inputs for the subsequent 1D flat premixed flame simulation for computing the LBV. Increased decomposition of NH_3 to form H radicals and increased production of O radicals by the plasma resulted in higher density of OH radicals, which in turn led to faster decomposition of NH_3 via NH_3 + OH reactions at low temperatures [14]. This caused a quicker rise in temperature and thus, an increase in LBV. Simultaneous NO_x reduction and extension of the lean blow-off (LBO) limits of ammonia flames were experimentally achieved in a premixed swirling flame in Choe et al. [15]. Two specific possibilities of chemical pathways were hypothesized in Choe et al. [15] to explain the observed NO_x reduction - i) Increased production of HO_2 could be responsible for driving up the NO and NO_2 consumption rates via $NO + HO_2 \rightarrow OH + NO_2$ and $NO_2 + HO_2 \rightarrow HONO + O_2$ and/or ii) increased production of NH_2, indicated by NH_2^* chemiluminescence, effecting the increased consumption of NO via $NO + NH_2 \rightarrow NNH + OH$ and $NH_2 + NO \rightarrow N_2 + H_2O$.

The current research is aimed at understanding the fundamental chemical kinetic pathways and gas heating modes that lead to shorter ignition delay, lower minimum ignition energy (MIE), and lower NO_x production of lean, rich and stoichiometric NH_3/air mixtures under constant pressure and constant volume conditions using an in-house zero-dimensional (0D) plasma assisted combustion solver. This directly leads to a discussion on the effects of different controllable parameters affecting overall non-equilibrium plasma assistance. Specifically, comparisons are made with thermal nanosecond and continuous power input systems representing conventional ignition technologies, to reveal the benefits of a nanosecond pulsed non-equilibrium plasma discharge over conventional methods. Moreover, unlike the previous research [9] involving combustion of ammonia and oxygen in an inert gas, the current work specifically focuses on plasma assisted combustion of ammonia in air. The presence of N_2 in air along with its atomic presence in NH_3 gives rise to interesting plasma chemical processes such as VT relaxation between pulses, increased NO_x formation during the plasma pulses (i.e., before ignition), and overall NO_x reduction after ignition, as compared to direct combustion of NH_3 in air. Moreover, it is worthwhile to probe into possible NH_3 reforming pathways facilitated by plasma to abate the extra fuel-bound NO_x that is produced due to NH_3. This can also help in approximately modeling systems where the plasma igniter is located immediately downstream of the fuel injector to reform NH_3 into N_2 and H_2.

This paper is structured as follows. Section 2.1 describes the details of the 0D PAC solver developed in-house for all the simulations described in this paper. A new plasma mechanism for ammonia-air discharge has been assembled in this work using reactions available in the literature (see Table A.1 in the supplementary materials) and is presented in Section 2.2. In addition, Section 2.2 presents the results of comparison between the experimental auto-ignition delays [16] and laminar flame speeds [17] and simulated results using five candidate combustion mechanisms for NH_3 in air [18–22], so as to choose a combustion mechanism to be coupled with the newly assembled plasma kinetic mechanism. Section 2.3 shows the verification and validation of the PAC solver with two different cases of plasma aided combustion [23,24]. Finally, the effects of the reduced electric field (E/N), equivalence ratio, pressure, pulse frequency and energy density per pulse on the ignition delay and NO_x emission for constant pressure and constant volume cases are discussed in detail in Section 3. Additionally, simulation of nanosecond thermal discharge and continuous thermal discharge with equivalent energy input haven been conducted to demonstrate the efficacy of non-equilibrium plasma for the ignition of ammonia-air mixtures, which is presented in Section 3.

2. Methodology

2.1. Plasma assisted combustion (PAC) solver

Zero-dimensional (0D) constant volume and constant pressure plasma assisted combustion models have been developed to simulate nanosecond discharges of non-equilibrium plasma in a gas mixture. A 0D plasma kinetics code, ZDPlasKin [25], is coupled with a 0D combustion kinetics code based on CHEMKIN-III [26] subroutines, which is functionally same as existing studies in the literature [23,27]. A schematic diagram of the solver is provided in the supplementary materials. The solver has been verified and validated, and the results are presented in Taneja and Yang [28] and in Section 2.3. The equations solved during the nanosecond pulses and the microsecond gaps between pulses are given by Eqs. (1)–(6), which will be discussed near the end of this section. This 0D model gives a quick and reasonably accurate estimate of all the other important variables, which are homogeneous throughout the bulk of the plasma for a glow discharge.

$$\frac{dN_i}{dt} = \sum_{j=1}^{j_{max}} Q_{ij}(t) \tag{1}$$

Q_{ij} in Eq. (1) stands for the contribution of reaction j to the net production / consumption of species i and N_i stands for the number density of species i.

A two-temperature model is used here, which assumes that ions, charged species and neutral species are in thermal equilibrium with each other, thereby sharing a common temperature, whereas, the electron temperature is to be determined by solving for the electron energy density by using the local mean energy approximation (LMEA) for evaluating the rate coefficients of electron impact reactions and the electron transport properties [29]. Species number densities, electron temperature, and gas temperature are updated at every time step during the plasma discharge pulses and gaps between adjacent pulses. However, combustion chemistry is assumed to be frozen during the discharge pulses as the time scales of plasma chemistry are two - three orders of magnitude shorter than the time scales of combustion chemistry. A constant reduced electric (E/N) field is used as a means to maintain the desired electron energy range based on the energy loss fractions of different electron impact reactions. This value is typically chosen to be the average value of the E/N field variation till breakdown. The duration of the pulse is made adaptive to ensure equal energy density deposition during every pulse. The values of E/N chosen are spread across the glow and nanosecond spark discharge regimes of practical low temperature plasma igniters, in order to assess its effect on the ignition delay and species number density evolution. The widely used double-precision variable-coefficient stiff ordinary differential equation solver (DVODE) [30] is used for temporal integration of the system with stiff governing ordinary differential equations (ODE's). The time step size is fixed at 0.01 ns during the discharge pulses and is allowed to gradually increase up to 5 ns during the gaps between adjacent pulses. A time-step independence study was done to arrive at these rather conservative estimates of time step sizes. Energy density values chosen in this work are similar to those obtained using 2D simulations of nanosecond glow and spark discharges in Tholin and Bourdon [31] and Rusterholtz et al. [32] (peak values of 0.5–1 J/cm^3 glow and spark discharges). However, effects of photoionization, convection and drift-diffusion, result in a spatial variation of number densities of electrons and ions, which in turn results in exponential distributions of energy densities in space. For instance, it decays exponentially by more than three orders of magnitude in a radial distance of less than 1 mm for typical nanosecond spark discharges in a pin-pin electrode setup. Since a 0D model does not account for these effects, an average estimate of 0.05 J/cm^3 per pulse was used. Moreover, energy densities higher than 0.1 J/cm^3 require longer pulse duration and result in very rapid ionization, thereby further driving up rates of electron impact processes, which necessitates time steps smaller than 0.1 picoseconds during and immediately after the plasma discharge to handle the increased stiffness of the reaction mechanism. Other than making the computations slower, this also poses numerical stability and convergence issues. An initial background ionization of $\sim 10^4$ electrons/cm^3 in a quasi-neutral mixture is assumed for all simulations, following Tholin and Bourdon [31]. This is done to provide a seed initial condition, mainly for the electron impact processes. Based on the E/N and energy density values, most pulses last for about 8−30 ns.

Governing equations for species number density evolution are described in Pancheshnyi et al. [25]. The constant pressure version of the gas energy equation is given by Eq. (2). Eq. (3) constitutes the source term, P_{gas}, of the gas energy equation. Eq. (4) is used to calculate the external electrical energy density per unit time (i.e., power density) supplied by the plasma. This gets divided into the kinetic power density of electrons - P_{elec} (Eq. (6)), that of the gas molecules - P_{gas} (Eq. (3)), and the chemical potential power density of all the molecules - P_{chem} (Eq. (5)). It is emphasized that the contributions of the creation/consumption of excited species and ions have been accounted in P_{chem} by adding their threshold energies to their respective ground states, in Eq. (5). For other ground state species, we simply use their respective formation enthalpies. E is the electric field strength, ν_e is the electron drift velocity, N_e is the electron number density, N_i is the number density of species i, γ is the ratio of specific heats, k_B is the Boltzmann constant, e is the electron charge, T_{gas} is the gas temperature, T_e is the electron temperature, and H_i' is the chemical potential of species i in Eqs. (1) - (6).

$$\frac{\gamma}{\gamma - 1} k_B \frac{d(N_{gas} T_{gas})}{dt} = P_{gas} \tag{2}$$

$$P_{gas} = P_{ext} - P_{chem} - P_{elec} \tag{3}$$

$$P_{ext} = e N_e E \nu_e \tag{4}$$

$$P_{chem} = \sum_{i=1}^{i_{max}} H_i' \frac{dN_i}{dt} \tag{5}$$

$$P_{elec} = \frac{3}{2} k_B \frac{d(N_e T_e)}{dt} \tag{6}$$

2.2. Plasma and combustion kinetic mechanism

The plasma kinetic mechanism consists of vibrational and electronic excitation, dissociation and ionization reactions of NH_3, N_2 and O_2, along with the corresponding electron-ion recombination, charge exchange and neutral ground state reactions. There are 53 species and 383 reactions in this mechanism. Specifically, air plasma chemistry mechanism was taken from Zhong et al. [33] which comprises of the vibrational and electronic states of N_2 and O_2, along with reactions of $O(^1D)$ and $O(^3P)$ which are crucial in determining the ignition delay at low temperatures [34]. Parametric studies have been done for a range of E/N values as different electron collision processes are dominant at different E/N values. For example, ionic species only play a role for very high values of E/N ($\sim 10^3$ Td and higher) as their threshold potentials are significantly higher than other processes [35]. Cross section databases for electron impact reactions of NH_3 were obtained from LxCAT online databases [36] provided by Hayashi et al. [37].

All the reactions involving NH_3 and the corresponding rate constants and references are listed in Table A.1 in the supplementary materials (Sec. A). All reactions of NH_3 with O_2, electrons, and other radicals have been taken from the plasma mechanism provided by Faingold and Lefkowitz [9] in their study on ignition of NH_3-O_2-He mixtures. The energy loss fraction of the second vibrational state of NH_3, i.e., $NH_3(v2)$, is significantly higher than that of the other states [38]. Moreover, most quenching reactions are only available for $NH_3(v2)$ in the literature. Hence, this study only considers one vibrational excited state of NH_3, i.e., $NH_3(v2)$. As will be discussed in Section 3, the interaction of NH_3 with the vibrational states of N_2 can have a significant impact on the ignition delay. This effect is predominantly seen at relatively lower values of the E/N field, where significant energy of the electrons goes into vibrational excitation of N_2. This effect is primarily modeled by reactions (5)−(12) (in Table A.1), obtained from Dreyer, Perner, and Roy [39], and then subsequently by reactions (82)−(84) (in Table A.1), obtained from Hovis and Moore [40]. Electronic excitation of NH_3 to NH_3(e1) and NH_3(e2) and subsequent dissociative quenching to form NH_2 and NH are lumped in two single-step reactions (2) and (3) (in Table A.1), as the second steps to form dissociated products are assumed to be very fast. Hence, the rates of these processes are assumed to be limited by the respective electronic excitation reactions, as is done in Faingold and Lefkowitz [9]. Reactions of the various NH_3 radicals among themselves, and with NH_3 and N_2, as given by reactions (53)−(66) (in Table A.1), are taken from Hong et al. [41].

Several candidate ammonia combustion mechanisms [18–22] were considered for coupling with the plasma mechanism. In order to assess the accuracy of available oxidation kinetics of NH_3, these mechanisms (hereafter named Otomo [18], Glarborg [19], Mei [20], Okafor [21], and Shrestha [22] mechanisms) were validated against experimental ignition delays (τ_{ig}) [16] and laminar flame speeds (S_L) [17]. Fig. 1(a) shows the validation results for ignition delays of $NH_3/O_2/Ar$ mixture at pressure 60 bar, temperatures ranging 1060−1140 K, and equivalence ratio (ϕ) of 0.5 (11.8% NH_3), measured in a rapid compression machine (RCM) [16]. The Glarborg, Mei, and Otomo mechanisms were found to satisfactorily capture the trend in experimental data. The under-prediction of τ_{ig} by these mechanisms for larger ignition delays could be attributed to the heat losses in the RCM, which were not considered in the simulations. Although lean conditions are more relevant to potential applications, the validation results for τ_{ig} at $\phi = 1$ and 2 can be found in the supplementary materials (see Fig. B.1).

Figure 1 (b) depicts the comparison of experimental laminar flame speeds S_L of NH_3/air mixtures [17] against model predictions at 298 K temperature and atmospheric pressure. The Glarborg mechanism was found to over-predict the flame speeds by a factor of two. All of the other mechanisms were found to satisfactorily follow the experimental trends and closer to experimental uncertainties. Additional results for the comparison of experimental S_L to that of the model predictions at various temperatures (323−448 K from the original experiments [17]) can be found in the supplementary materials (see Fig. B.2).

Among the available NH_3 oxidation mechanisms, Mei and Otomo models follow the experimental trends closely. However, between them, the Mei model captured the laminar flame speeds S_L more accurately within the experimental uncertainties. In addition, the Mei mechanism was found to better predict the experimental results of NO in a jet-stirred reactor (JSR) [42] among the available mechanisms (see Fig. B3 in supplementary materials). Thus, Mei mechanism [20] has been chosen as the reference combustion mechanism for NH_3 in this study. The combustion mechanism is made up of 33 species and 258 reactions, with some species in common with the plasma mechanism. Mei mechanism is then coupled with the plasma mechanism in a consistent manner to obtain a coupled plasma-combustion mechanism. The coupled mechanism together consists of 73 species and 640 reactions. The mechanism files along with the cross section databases used for electron impact reactions are provided as supplementary materials.

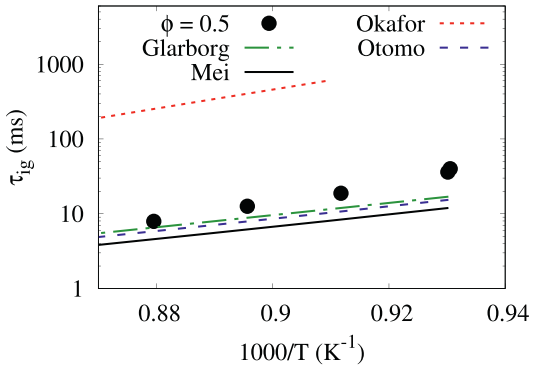

(a) Ignition delay times

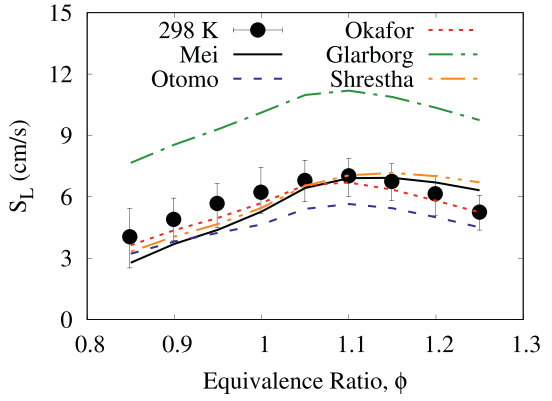

(b) Laminar flame speeds

Fig. 1. Comparison between experimental and simulated results of (a) ignition delay times τ_{ig} at $\phi = 0.5$ and (b) laminar flame speeds S_L at 298 K, using different ammonia combustion mechanisms. The lines represent simulated results using different mechanisms [18–22] and symbols represent experimental data for τ_{ig} [16] and S_L [17].

2.3. Validation of the 0D PAC code

Plasma discharge experiments can be used to validate the 0D PAC code developed in this work. Such experiments are conducted at very low pressures and temperatures so that combustion chemistry at these conditions is almost frozen, thereby making use of well established discharge kinetics of select plasma chemistry. In order to validate the 0D PAC code developed in this work, the time dependent temperature and H_2O profiles of H_2/O_2/He mixtures undergoing 1500 pulses of 30 kHz nanosecond pulse discharges at an initial pressure of 60 Torr and temperature 300 K were employed from Mao et al. [23]. The value of E/N was fixed to 100 Td (1 Td = 10^{-17} V cm^2) in this simulation, as the average value of experimental E/N profile was found to be 100 Td during the discharge pulse. Figure 2 shows the experimental [23] and simulated profiles of temperature and H_2O. The simulations were performed considering the conductive heat loss term to account for the drop in experimental temperature profile. Moreover, the simulations were performed at both a fixed supply of pulse energy (E_p) (dashed red lines) and a varying pulse energy (dotted green lines) to see the

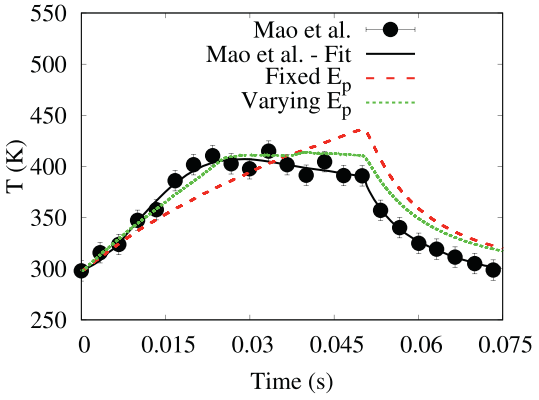

(a) Temperature profile

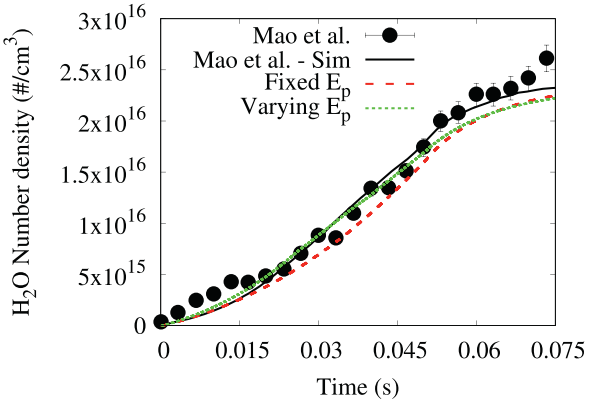

(b) Number density of H_2O

Fig. 2. Comparison between experimental and simulated results of (a) temperature evolution and (b) number densities of H_2O of H_2/O_2/He mixtures, undergoing 1500 pulses of 30 kHz nanosecond pulse discharges at an initial pressure of 60 Torr and temperature 300 K. The solid black lines represent the simulations in Mao et al. [23] and symbols represent experimental data from Mao et al. [23]. Dashed red lines - fixed pulse energy, dotted green lines - varying pulse energy in the present work.. (For interpretation of the references to color in this figure legend, the reader is referred to the web version of this article.)

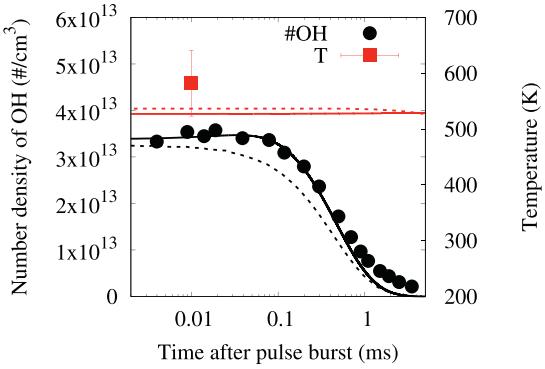

(a) $\phi = 0.06$

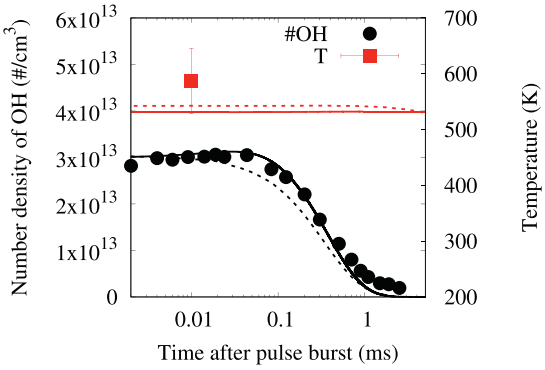

(b) $\phi = 0.12$

Fig. 3. Results of simulated temperature evolution and number densities of OH radical of H_2/air mixtures after a 50-pulse burst at (a) $\phi = 0.06$ and (b) $\phi = 0.12$ for an initial pressure 100 Torr and temperature 500 K. The lines represent simulated results (solid lines - current study, dashed lines - original study) and symbols represent experimental data from Nagaraja et al. [24].

resulting improvements in simulated number densities of H_2O by accurately matching the temperature profile. For the varying E_p case, two different pulse energies were used: a larger pulse energy up to 0.025 seconds and a smaller pulse energy from 0.025−0.5 seconds to match the change of slope in the temperature profile in Fig. 2(a). From Fig. 2(a), the temperature profile is found to closely follow the experimental trend for the varying E_p case. The temperature profile for fixed E_p over-predicts the temperature at end of discharge burst (0.05 s) by about 50 K. This error can be attributed to the inevitable inaccuracies of incorporating the heat loss term in the present code. Nevertheless, both fixed and varying E_p simulations were able to satisfactorily predict the number densities of H_2O (see Fig. 2(b)).

To further validate the code, simulations were performed for H_2/air mixtures at lean conditions ($\phi = 0.06$ and 0.12) at initial pressure 100 Torr and temperature 500 K. The model predictions of OH number densities and temperature were compared with experimental data [24] after a 50-pulse burst at 10 kHz repetition rate (see Fig. 3(a) and (b) for $\phi = 0.06$ and 0.12, respectively). The solid lines correspond to the present validation results whereas, the dashed lines represent the simulated results in the original work [24]. The symbols represent experimental data with associated uncertainty. The results depict satisfactory predictions of OH profiles within experimental uncertainties, when the simulations were performed to match the temperature profile of the original study. These results, along with the validation results in Fig. 2 asserts the validity of the present numerical model. Further model validation using experimental ignition delay times [23,24] can be found in the supplementary materials (see Fig. D.1 and D.2).

3. Results and analysis

For ammonia to become a mainstream fuel, several key challenges associated with its combustion must be addressed. Long ignition delays due to higher ignition energy requirements and high NO_x production are two of the primary challenges that this work aims to address using non-equilibrium plasma. PAC with ammonia under varied set of operating conditions is investigated for constant volume and constant pressure 0D homogeneous reactors. Constant volume (CV) reactors are chosen to approximately represent combustion in internal combustion (IC) engines, which can crudely be modeled using an Otto cycle approximation. Similarly, constant pressure (CP) reactors are chosen to approximately represent the heat addition process in gas turbines based on the Brayton cycle assumption. The results presented here are typically at atmospheric pressures or slightly higher, which may not be representative of these practical combustion systems. But the goal is to understand the fundamental PAC chemical kinetics of ammonia, first at atmospheric pressures, rather than target applications. Hence, this numerical research could become a reference for fundamental experimentalists interested in investigating PAC kinetics

Table 1
Different cases of constant volume (CV) 0D simulations used in the present study. (Initial Pressure = 1 atm., Initial Temperature = 800 K).

Parameters - Constant Volume (CV)					
No.	E/N	ϕ	Frequency (kHz)	Energy density per pulse (J/cm^3)	No. of pulses
CV1	150	1.0	100	0.05	10
CV2	150	1.0	30	0.05	10
CV3	150	0.5	100	0.05	10
CV4	550	1.0	100	0.05	10
CV5	150	1.0	100	0.025	10
CV6	0	1.0	100	0.05	10
CV7	0	1.0	-	1.3 (> 0.5) (total)	Continuous

Table 2
Different cases of constant pressure (CP) 0D simulations used in the present study. (Initial Temperature = 800 K, Pulse Frequency = 100 kHz).

Parameters - Constant Pressure (CP)					
No.	E/N	ϕ	Pressure (atm)	Energy density per pulse (J/cm^3)	No. of pulses
CP1	150	1.0	1.0	0.05	10
CP2	150	1.0	3.0	0.05	20
CP3	150	1.2	1.0	0.05	10
CP4	550	1.0	1.0	0.05	10
CP5	150	0.5	1.0	0.05	10
CP6	0	1.0	1.0	0.05	10
CP7	0	1.0	1.0	1.3 (> 0.5) (total)	Continuous

of ammonia with nanosecond pulsed discharges, that are generally easier to do at atmospheric pressures, than higher pressures. The applications mentioned here simply motivate the choice of the model and parameter approximations (i.e., reactor type, values of the reduced electric field, equivalence ratios, etc.). It should also be noted that the 0D model is not a perfect representation of such applications as effects of bulk gas recirculation, turbulence, drift-diffusion, photoionization etc. can not be modeled. While it is possible to model the effects of species transport and convective heat loss approximately in these 0D reactors by including certain source terms with some characteristic time scales associated with these processes, we consider adiabatic reactors for this study as those length/time scales often require a lot of tuning which introduces needless uncertainties for this fundamental study.

Equivalence ratio (ϕ), reduced electric field (E/N), pressure, pulse frequency and energy density per pulse are chosen as the main parameters to perform a parametric study to understand how each of them affects the ignition delay time. All parametric cases simulated using constant volume and constant pressure reactors (CV1−CV5 and CP1−CP5 in Tables 1 and 2) are compared among themselves, and with two additional baseline cases (CV6/CP6 for nanosecond thermal energy deposition and CV7/CP7 for continuous thermal energy deposition). Both these additional cases replace the effect of plasma using a heat source term. CV6/CP6 models nanosecond pulsed heat source, whereas CV7/CP7 models traditional heat kernel assisted combustion (e.g. equilibrium arc ignition), where a heat source of magnitude $\dot{Q}$ is applied for a certain interval τ, such that the total energy deposited, $\int_0^\tau \dot{Q}dt$ is equal to a constant predetermined value. The various cases considered in this study are tabulated in Tables 1 and 2 along with case numbers, which are used for discussion in Sections 3.1.1 to 3.1.5 (for ignition delays) and Sections 3.2.1 to 3.2.4 (for NO_x production). The values chosen for all the parameters are based on practical considerations such as typical voltages applied to the electrodes, common and desired equivalence ratios of the combustion mixtures, range of frequencies in most practical plasma igniters, energy density per pulse corresponding to the nanosecond glow or spark discharges used at atmospheric pressure [31,32], and the number of pulses are adjusted accordingly to achieve ignition delays that are commonly desirable for engines and gas turbines.

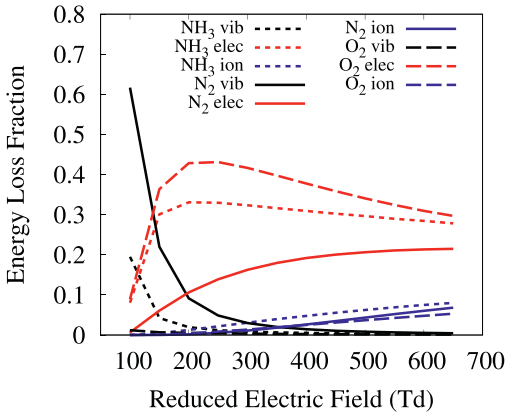

Fig. 4. Electron energy loss fractions of NH_3, N_2, O_2 species at different reduced electric fields (E/N).

3.1. Ignition delay times

3.1.1. Effect of reduced electric field (E/N)

As is shown in Fig. 4, the percentage of electron energy deposited in different modes depends on the reduced electric field (E/N). In Fig. 4, only the vibrational and electronic excitation, and ionization modes are shown since very low energy (less than 1%) goes into the rotational modes in the desired range of E/N (100−600 Td). Moreover, the energy loss fractions for all the vibrational and electronic excitation, and ionization processes are summed individually for every species. Since the vibrational energy contribution is relatively higher at lower values of E/N (100−200 Td), vibrational-to-translational relaxation (VT relaxation) and kinetics associated with the vibrational states of N_2 and NH_3 are expected to play a major role in determining the ignition delays at 100−200 Td. As observed in Fig. 5, a difference of about an order of magnitude is observed in the ignition delay, when E/N is increased from 150 Td (CV1) to 550 Td (CV4). Although the number density of OH radical is found to be similar between CV1 and CV4 (red lines in Fig. 5), the rise in temperature during pulses were observed to be higher in case of CV1 when compared to

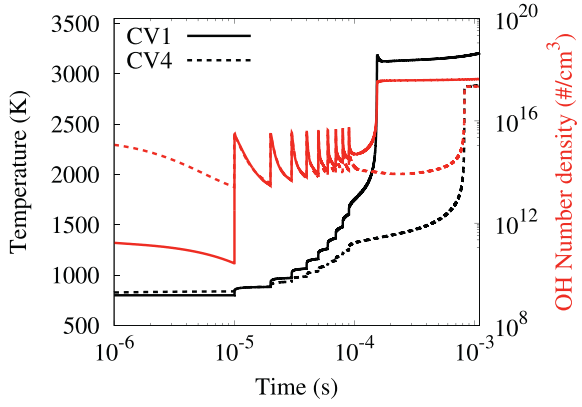

(a) Temperature and OH

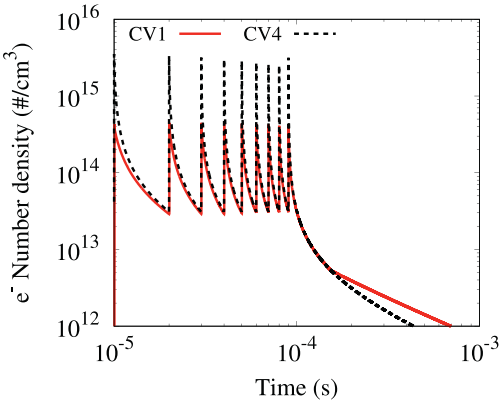

(b) Electron number density

Fig. 5. Evolution of (a) temperature (black lines) and number density of OH radical (red lines) for E/N = 150 Td (CV1, solid lines) and 550 Td (CV4, dashed lines) and (b) the electron number density (CV1 - solid red lines and CV4 - dashed black lines) in a constant volume 0D reactor. Note - Plots in this paper start from 10^{-5} s to avoid crowded plots at larger times because of the logarithmic scale.. (For interpretation of the references to color in this figure legend, the reader is referred to the web version of this article.)

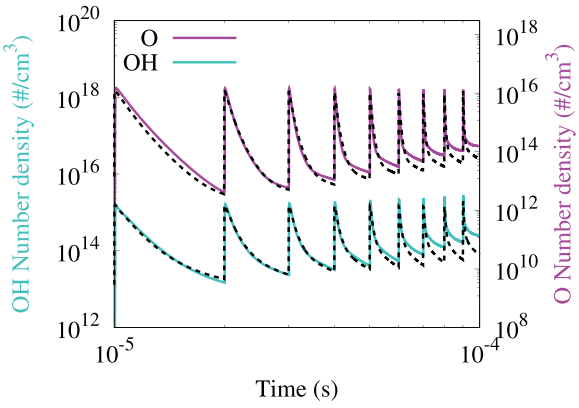

Fig. 7. Number densities of OH radical (turquoise line) and O radical (magenta line) at E/N = 150 Td (solid turquoise/magenta lines) and 550 Td (dashed black lines) in a constant volume 0D reactor.

CV4 (black lines in Fig. 5). In order to understand the slow rise in temperature and the consequent increase in ignition delays at 550 Td, path flux analyses have been performed for the consumption of NH_3 during the last pulse. Path flux analysis of CV1 (E/N = 150 Td) and CV4 (E/N = 550 Td), as shown in Fig. 6, specifically analyzes the impact of relaxation of $N_2(v1 - v8)$ and $NH_3(v2)$ to their respective ground states. At 150 Td, it is observed from Fig. 6(a) that about 41% of NH_3 is being consumed through the vibrational-vibrational (VV) exchange reaction of N_2 and NH_3 (i.e., $N_2(v1 - v8) + NH_3 \rightarrow N_2 + NH_3(v2)$) to produce $NH_3(v2)$, which predominantly relaxes back to NH_3 ($\sim$ 98%). In addition, another 40.5% of NH_3 gets consumed through an electron impact reaction to produce $NH_3(v2)$. However, at 550 Td (Fig. 6(b)), only 0.2% of NH_3 is consumed through the VT relaxation of N_2. About 34% of NH_3 undergoes electron impact to produce $NH_3(v2)$, of which only 57% relaxes back to NH_3. Moreover, the consumption of NH_3 via electron impact reactions to produce NH_2 (36%) and NH (18%) is observed to be higher at 550 Td. These observations justify the dominance of VT relaxation reactions at 150 Td and their insignificance at 550 Td.

Figure 7 shows the number densities of important radicals (O and OH) at both 150 and 550 Td. It can be seen that the amount of O and OH radicals are similar between 150 and 550 Td and hence

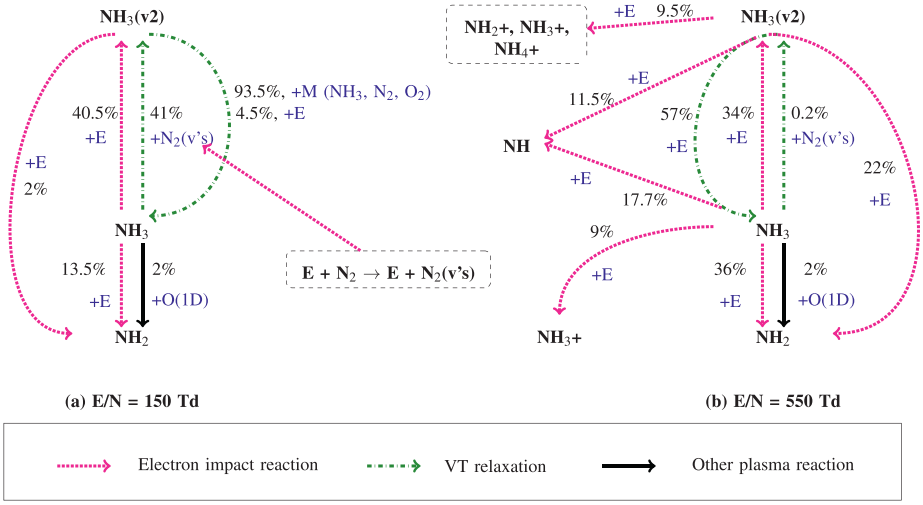

Fig. 6. Path flux analysis for the consumption of NH_3 during the last pulse at (a) E/N = 150 Td (CV1) and (b) E/N = 550 Td (CV4) in a constant volume 0D reactor. The flux percentages are calculated relative to the consumed parent species.

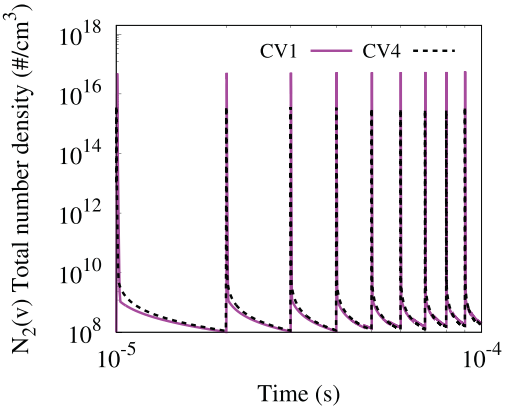

(a) Total N_2(v) number density

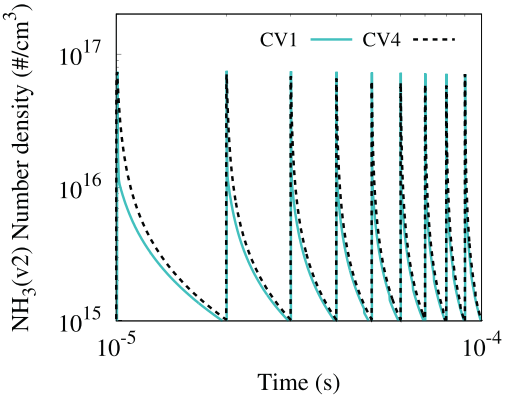

(b) NH_3(v2) number density

Fig. 8. Number densities of (a) all the vibrational excited states of N_2 species (represented by $N_2(v)$) and (b) vibrational excited state of NH_3 species ($NH_3(v2)$) at E/N = 150 Td (CV1, solid turquoise/magenta lines) and 550 Td (CV4, dashed black lines) in a constant volume 0D reactor.

Table 3
List of reactions involved in the consumption of NH_3 and their corresponding enthalpies of reaction.

Reaction	Enthalpy of reaction, ΔH_r (kJ/mol)
$E + NH_3 \rightarrow E + NH_2 + H$	456.1
$O(^1D) + NH_3 \rightarrow OH + NH_2$	28.1
$N_2(v1) + NH_3 \rightarrow N_2 + NH_3(v2)$	-17.6
$N_2(v2) + NH_3 \rightarrow N_2 + NH_3(v2)$	-46.5
$N_2(v3) + NH_3 \rightarrow N_2 + NH_3(v2)$	-75.5
$N_2(v4) + NH_3 \rightarrow N_2 + NH_3(v2)$	-94.8
$N_2(v5) + NH_3 \rightarrow N_2 + NH_3(v2)$	-123.7
$N_2(v6) + NH_3 \rightarrow N_2 + NH_3(v2)$	-152.6
$N_2(v7) + NH_3 \rightarrow N_2 + NH_3(v2)$	-181.6
$N_2(v8) + NH_3 \rightarrow N_2 + NH_3(v2)$	-200.9

do not explain the higher reactivity observed at 150 Td. Therefore, it is hypothesised that the dominance of VT relaxation at 150 Td (as observed in the path flux diagram, Fig. 6) contributes to the increased reactivity at 150 Td. To ascertain this hypothesis, the number densities of the total vibrational states of N_2 (i.e., $N_2(v1 - v8)$) and $NH_3(v2)$ are depicted in Fig. 8. It is observed that at 150 Td, the peak number density of $N_2(v1 - v8)$ is about an order of magnitude higher compared to that at 550 Td, and is in accordance with the dominance of vibrational energy contribution at 150 Td. Table 3 portrays the major reactions which consumes NH_3 and their corresponding reaction enthalpies (ΔH_r). A negative value of ΔH_r implies the reaction to be exothermic. From Table 3, it can

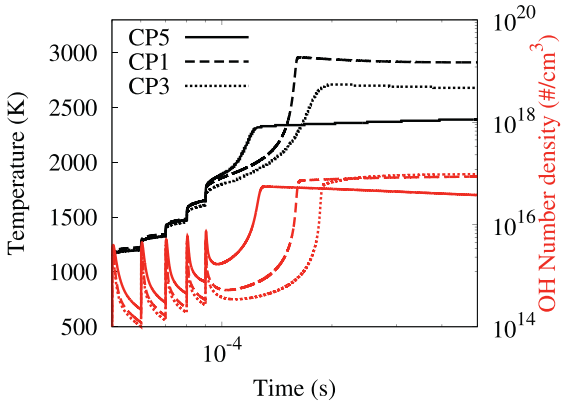

Fig. 9. Evolution of temperature (black lines) and number density of OH radical (red lines) at $\phi = 0.5$ (CP5, solid lines), $\phi = 1.0$ (CP1, dashed lines), and $\phi = 1.2$ (CP3, dotted lines) in a constant pressure 0D reactor. (For interpretation of the references to color in this figure legend, the reader is referred to the web version of this article.)

be observed that the reactions involving the production of NH_2 are endothermic, whereas, the VT relaxation reactions of nitrogen that results in the production of $NH_3(v2)$ (through $N_2(v1 - v8)$) are exothermic.

Thus the dominance of the VT relaxation at 150 Td (41%, $NH_3 \longrightarrow NH_3(v2)$) over 550 Td (0.2%, $NH_3 \longrightarrow NH_3(v2)$) implies that about 41% of NH_3 is consumed through exothermic pathways at 150 Td, resulting in significant heating up of the mixture during the plasma discharges, as seen from the temperature profiles in Fig. 5 (black solid lines). However at 550 Td, the consumption of NH_3 through exothermic VT relaxation pathways is insignificant (0.2%) and is consumed mainly through endothermic pathways to produce NH_2 and NH, thereby resulting in a lower rate of heating during the plasma discharges as shown in Fig. 5 (black dashed lines). This increased heating due to VT relaxation reactions favor the endothermic decomposition of fuel to smaller species and their subsequent oxidation, thereby inducing the increased reactivity at 150 Td compared to 550 Td.

3.1.2. Effect of equivalence ratio

Temperature and OH number density for lean ($\phi = 0.5$, CP5), stoichiometric (CP1) and rich ($\phi = 1.2$, CP3) mixtures of NH_3 and air are plotted in Fig. 9. Despite almost equal production of OH during the plasma pulses, the consumption rates of OH radical during the gaps are much smaller for case CP5 (lean), as compared to cases CP1 (stoichiometric) and CP3 (rich). Thus, at the end of 10 plasma pulses (1×10^{-4} s), case CP5 is found to have an accumulated OH density, which is almost thrice as compared to CP1 and CP3. This observation suggests the role of OH consumption pathways on the reduced reactivity of the rich mixture.

In order to ascertain the role of OH consumption in lowering the reactivity of the rich mixture, sensitivity and species consumption analyses were performed for ignition delays and OH consumption respectively. Fig. 10 shows a sensitivity analysis on the ignition delays of $NH_3/O_2/N_2$ mixtures at 1 bar and 1600 K. A positive sensitivity coefficient reflects an increase in ignition delay (reduced reactivity) when the rate of the reaction is increased. It can be observed that the fuel-specific H-abstraction reactions $NH_3 + OH \rightarrow NH_2 + H_2O$ and $NH_3 + H \rightarrow NH_2 + H_2$ exhibit a positive sensitivity coefficient, revealing the inhibiting nature of these reactions. This is due to the replacement of highly reactive OH and H radical with lesser reactive NH_2 in the radical pool. Based on this observation, the consumption pathways of OH during the last inter-pulse gap ($\sim 1 \times 10^{-4}$ s) were probed into, to understand the cause of difference in its number density between the three cases (see Fig. 11).

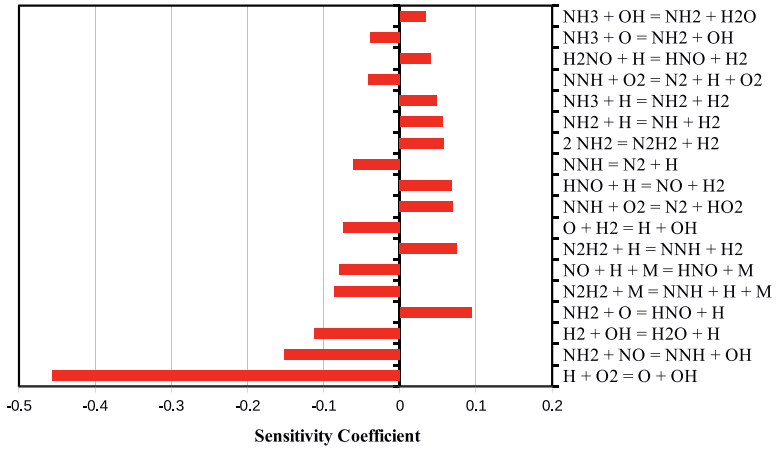

Fig. 10. Sensitivity analysis of $NH_3/O_2/N_2$ mixtures to the ignition delays at 1 bar and 1600 K. A positive sensitive coefficient reflects an increase in the ignition delay (reactivity inhibiting reaction).

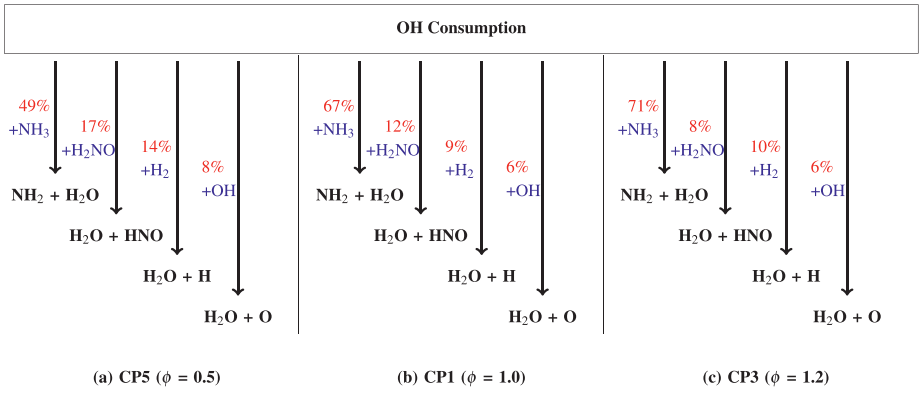

Fig. 11. Consumption pathways of OH radical after the last pulse at (a) $\phi = 0.5$ (CP5), (b) $\phi = 1.0$ (CP1), and (c) $\phi = 1.2$ (CP3) in a constant pressure 0D reactor. The flux percentages are calculated relative to the consumed parent OH radical.

From Fig. 11, it can be seen that $NH_3 + OH \rightarrow NH_2 + H_2O$ is the major reaction consuming OH radicals. About 49% of OH gets consumed through this pathway in case CP5 at a rate 8,150 mol/m^{3}s, as compared to 67% and 71% in cases CP1 (20,378 mol/m^{3}s) and CP3 (33,468 mol/m^{3}s), respectively. The least consumption rate of OH radicals for the case CP5 can be attributed to the comparatively lower concentration of NH_3 (fuel) to begin with, in the case of CP5 as compared to CP1 and CP3.

Thus, the H-abstraction reaction $NH_3 + OH \rightarrow NH_2 + H_2O$ is found to inhibit the reactivity of rich mixtures. Similar analysis on the consumption of H radicals reveal $NH_3 + H \rightarrow NH_2 + H_2$ to be the dominant H destruction pathway with destruction rates of 14,840, 63,880, and 76,473 mol/m^{3}s for lean, stoichiometric, and rich cases respectively. On account of the dominance of these H-abstraction reactions (thereby destroying H and OH radical pool) in case of CP3 ($\phi = 1.2$), compared to CP1 ($\phi = 1.0$) and CP5 ($\phi = 0.5$), the fuel-rich mixture (CP3) is observed to exhibit lowest reactivity, followed by stoichiometric (CP1) and fuel-lean mixtures (CP5). The other reactions consuming OH radicals (see Fig. 11) were not found to significantly differ between the three cases, as compared to the H-abstraction reactions involving H and OH.

3.1.3. Effect of pressure

Many practical combustion systems often operate at pressures above atmospheric, and hence, it is worthwhile to explore how higher pressures affect ignition delays. It should be noted that the high pressure case, CP2, uses 20 pulses, unlike the reference case CP1, which only uses 10 pulses. However, the energy density per pulse is maintained equal, i.e., 0.05 J/cm^3. Thus, CP2 (3 atm) has twice the overall energy deposition as compared to CP1. This was required since 10 pulses were inadequate for igniting the lesser-reactive mixture at 3 atm in the CP2 case. Hence, to maintain pressure as the only parametric difference between the two cases until the 10th pulse, increasing the number of pulses for CP2 provided a basis for fairer comparison. Fig. 12 depicts the evolution of temperature and number density of OH radical for cases CP1 (1 atm)

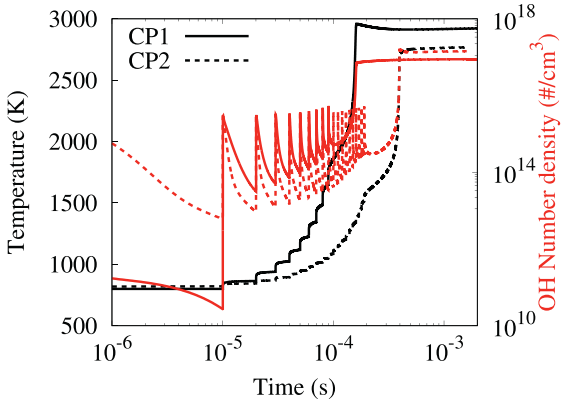

Fig. 12. Evolution of temperature (black lines) and number density of OH radical (red lines) at pressures of 1 atm (CP1, solid lines) and 3 atm (CP2, dashed lines) in a constant pressure 0D reactor.. (For interpretation of the references to color in this figure legend, the reader is referred to the web version of this article.)

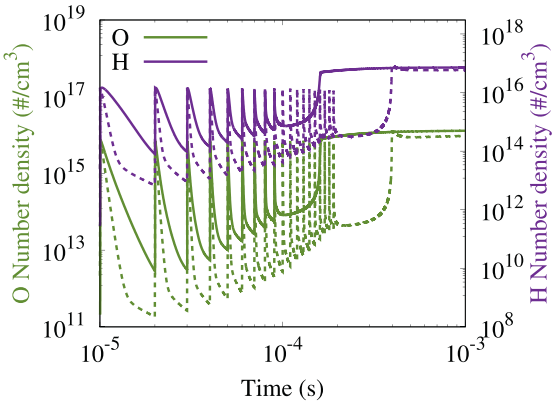

(a) Radicals

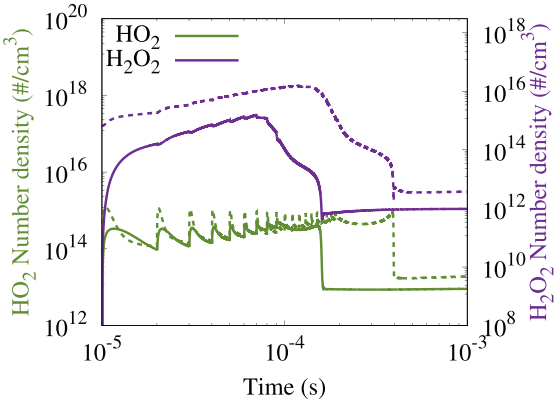

(b) Meta-stable species

Fig. 13. Number densities of (a) important radical species (H and O radicals, violet and green lines, respectively) and (b) meta-stable species (H_2O_2 and HO_2, violet and green lines, respectively) at pressures of 1 atm (solid violet/green lines) and 3 atm (dashed violet/green lines) in a constant pressure 0D reactor.. (For interpretation of the references to color in this figure legend, the reader is referred to the web version of this article.)

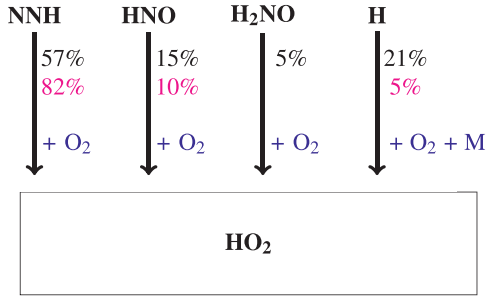

Fig. 14. Production pathways of HO_2 after the sixth pulse at pressures of (a) 1 atm (CP1 – values in black) and (b) 3 atm (CP2 – values in pink) in a constant pressure 0D reactor. The flux percentages are calculated relative to the produced HO_2 species.

and CP2 (3 atm). A 3x longer ignition delay was observed in case of CP2 as compared to case CP1 (see Fig. 12) despite depositing twice the overall energy in CP2. The lower reactivity of case CP2 can be observed from the lower number densities of reactive radicals such as OH, O and H from Figs. 12 and 13(a) at the beginning of each plasma pulse. This can be attributed to an important three body recombination reaction, $H + O_2 + M \rightarrow HO_2 + M$, which is known to be dominant at higher pressures. Figure 14 shows the difference in production pathways for HO_2 for CP1 (1 atm)

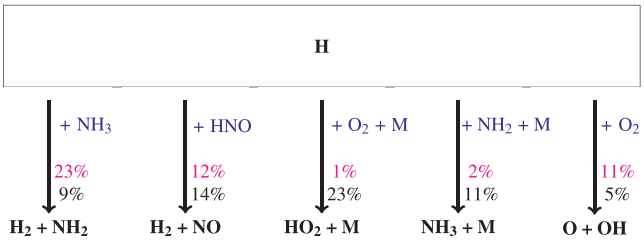

Fig. 15. Consumption pathways of H radical after the sixth pulse at pressures of (a) 1 atm (CP1 – values in black) and (b) 3 atm (CP2 – values in pink) in a constant pressure 0D reactor. The flux percentages are calculated relative to the consumed H species.

and CP2 (3 atm) cases. NNH and HNO (fuel derived species) react with O_2 to produce almost 92% of the total number density of HO_2 at 1 atm, whereas only 5% is produced by consuming H radicals. However, at 3 atm, 21% of HO_2 is produced from H radicals by $H + O_2 + M \rightarrow HO_2 + M$ and only 72% is produced from NNH and HNO. This is also noticeably evident from an order of magnitude increased production of HO_2 (and consequently H_2O_2 due to $HO_2 + HO_2 \rightarrow H_2O_2 + O_2$) for CP2 as compared to CP1, as is shown in Fig. 13(b). Another chain terminating reaction, $H + NH_2 + M \rightarrow NH_3 + M$, also contributes towards quicker depletion of H radicals at high pressures. The influence of these pressure dependent recombination reactions at higher pressures inhibits the chain branching process of $H + O_2 \rightarrow O + OH$ by competing for consumption of H, thereby reducing the reactivity of the mixture at high pressures (CP2). Figure 15 highlights this fact, specifically for the increased consumption of H radicals at higher pressures. This important chain branching pathway of $H + O_2 \rightarrow O + OH$ produces a lesser proportion of OH at higher pressures (only 1% of OH in CP2 as compared to 13% in CP1), further reducing reactivity. Furthermore, $NH_3 + OH \rightarrow NH_2 + H_2O$ is more dominant in consuming OH at high pressures (90% for CP2 vs 79% in CP1), which is also a reactivity inhibiting step as OH is a more reactive radical than NH_2 to control ignition.

3.1.4. Effect of pulse energy and pulse frequency

A rather straightforward (and expected) trend in ignition delay was observed when the energy density per pulse and pulse frequency were altered. Increasing either of energy density and pulse frequency resulted in shorter ignition delays simply because all the fundamental processes responsible for ignition, as discussed before, were accelerated. The details and resultant plots of these effects are provided in the supplementary materials.

3.1.5. Effect of nanosecond pulsed non-equilibrium plasma

The primary effect of non-equilibrium plasma chemistry is highlighted by comparing results with the two baseline cases, CP6 (nanosecond thermal discharge) and CP7 (continuous thermal discharge). CP7 is representative of conventional equilibrium arc discharges used in internal combustion engines and gas turbines, whereas CP6 is an ideal pulsed discharge case, where all the energy is used for direct gas heating, within a few nanoseconds. The latter could be thought to represent a pulsed laser ignition method. The total time for which the source is active is maintained at 10^{-4} s for all cases. The case CP6 is simulated using the in-house PAC code, where, the reduced electric field (E/N) is set to 0 Td and a fixed pulse duration. A uniform power density is applied to ensure equal energy density of 0.05 J/cm^3 for each of the ten pulses, same as CP1. The CP7 case is simulated by solving constant heat source based ignition with Cantera [43], where the power density is set to 1.3×10^4 W/cm^3. Thus, the total energy density for both CP1 (nanosecond plasma discharge) and CP6, after 10 pulses is 0.5 J/cm^3, whereas it is 1.3 J/cm^3 for CP7. The increased energy

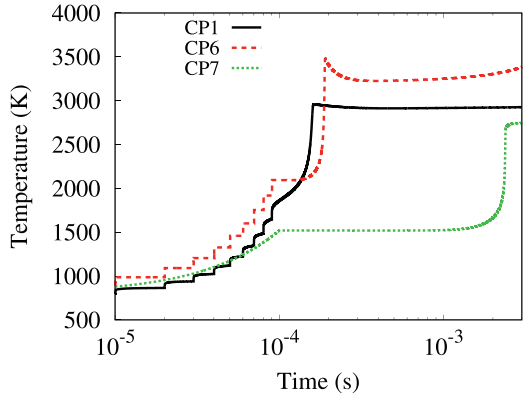

(a) Temperature

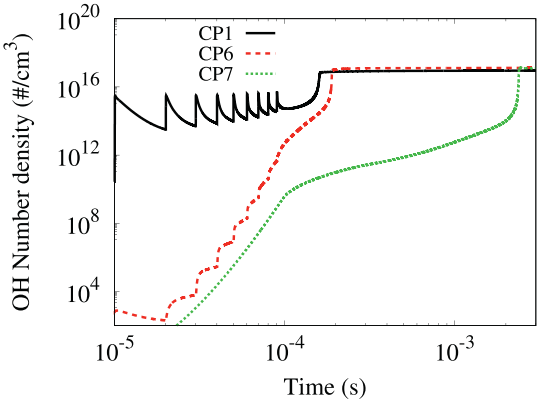

(b) OH Number density

Fig. 16. Evolution of (a) temperature and (b) number density of OH radical for nanosecond plasma energy deposition (CP1, solid black lines), nanosecond thermal energy deposition (CP6, dashed red lines), and continuous thermal energy deposition (CP7, dotted green lines) in a constant pressure 0D reactor. (For interpretation of the references to color in this figure legend, the reader is referred to the web version of this article.)

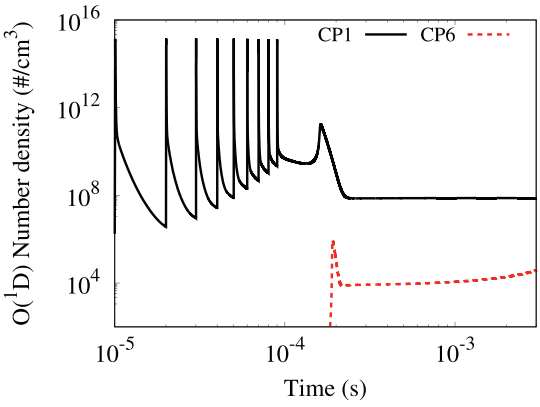

(a) O(^{1}D) Number density

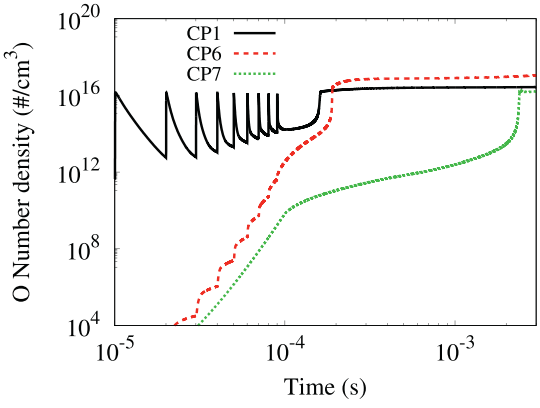

(b) O Number density

Fig. 17. Number densities of (a) O(^1D) and (b) O radical for nanosecond plasma energy deposition (CP1, solid black lines), nanosecond thermal energy deposition (CP6, dashed red lines), and continuous thermal energy deposition (CP7, dotted green lines) in a constant pressure 0D reactor. (For interpretation of the references to color in this figure legend, the reader is referred to the web version of this article.)

density for CP7 is used to obtain a significantly shorter delay, even though it still is an order of magnitude longer than those of CP1 and CP6 cases. Based on our sensitivity tests, different combinations of heat source duration and power densities resulted in almost the same ignition delay for CP7.

A clear advantage of using nanosecond pulsed supply of energy over a continuous supply of energy can be seen in Fig. 16, as CP1 is observed to have the shortest ignition delays, and CP6 also ignites much faster than CP7. Despite the longer ignition delay, the temperature rise after each pulse is higher for case CP6 (nanosecond thermal) as compared to case CP1 (nanosecond plasma). This is because all the energy is deposited as heat in the former, whereas it is distributed to facilitate different chemical processes and increase the electron and gas temperatures for the latter case. The advantage of plasma chemistry can be seen by comparing the number densities of O, OH and O(^1D) radicals in Figs. 16(b) and 17, which are found to be considerably higher for CP1 compared to CP6 and CP7. However, in case of CP6, the heat source was sufficient to raise the temperature to around 2000 K, i.e., close to the ignition temperature. Thus, temperature rise is the major driver to enhance the overall reactivity of the mixture in the case of CP6. When the heat source per pulse times the number of pulses is further reduced, for both nanosecond plasma and nanosecond thermal discharges, one can see how plasma kinetics help in building a radical pool at low temperatures, which majorly drives the mixture to ignition. Finally, even though the pathways for O and OH production are similar (not identical; as is shown in Fig. 18 (b) and (c)), the overall rates and densities of these radicals are quite different for cases CP6 and CP7. This is apparent from Figs. 16 (b) and 17 (b). For instance, the major O production pathways for CP6 and CP7 are $NH_2 + O_2 \rightarrow O + H_2NO$ and $H + O_2 \rightarrow O + OH$. The O radical production rates are 7.22×10^{-5} moles/(m^3·s) and 8.36×10^{-6} moles/(m^3·s) for CP6 and CP7, respectively. Thus, a difference of one order of magnitude was observed. Also, the major OH radical production pathways are $NH_3 + O \rightarrow NH_2 + OH$ for CP6 and $NH_2 + O \rightarrow NH + OH$ for CP7. The rates for OH production are 7.04×10^{-5} moles/(m^3·s) and 5.06×10^{-12} moles/(m^3·s) for CP6 and CP7, respectively. Thus, a difference of seven orders of magnitude was observed. These instantaneous rates are obtained at approximately 50 μs, which is half-way during the energy deposition periods for both the cases. The consequences are 2× and 20× shorter ignition delays for the nanosecond plasma case as compared to the nanosecond thermal case and the continuous thermal discharge case, respectively.

Production paths for OH radical were probed into, before the completion of the last pulse for cases CP1 (nanosecond plasma) and CP6 (nanosecond thermal), and at the same time instant for CP7 (continuous thermal) and is given in Fig. 18. Figure 18(a) shows that direct electron impact reaction of O_2 and the

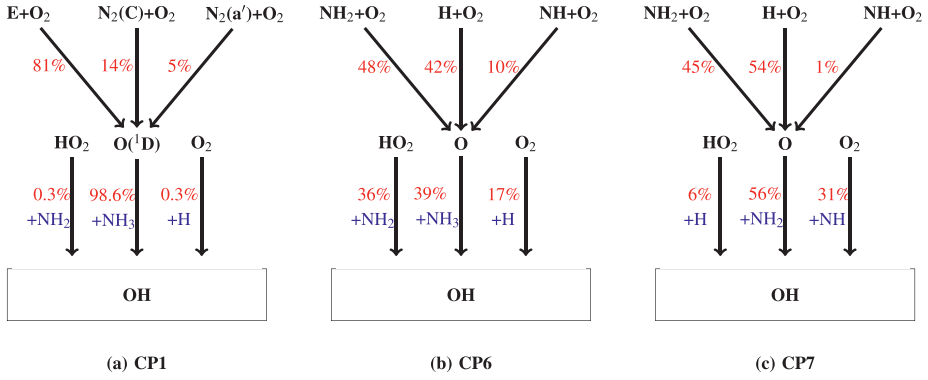

Fig. 18. Production pathways of OH radical during the last pulse for (a) nanosecond plasma energy deposition (CP1), (b) nanosecond thermal energy deposition (CP6), and (c) continuous thermal energy deposition (CP7) in a constant pressure 0D reactor. The flux percentages are calculated relative to the produced OH species.

recombination of the electronic states of N_2 ($N_2(C)$, $N_2(a')$) with O_2 to be major channels of $O(^1D)$ production, which is in turn responsible for majority of the OH production in case of CP1. For both the thermal ignition cases (CP6 and CP7), O, HO_2 and O_2 are the dominant species for OH production, with the common chain branching reaction, $H + O_2 \rightarrow O + OH$ playing a primary role in the production of O and OH radicals. The production of OH radical from O, O_2, and HO_2, however, is limited in CP6 and CP7 (see Fig. 16(b)), as the amount of O radical produced in these cases is far lesser than that produced for the case of CP1 (see Fig. 17(b)). Moreover, CP6 and CP7 do not produce $O(^1D)$ in considerable amounts when compared to CP1, owing to the lack of activated plasma chemistry in the former ones. Nevertheless, trace quantities of $O(^1D)$ species are produced in the nanosecond thermal discharge case as well, especially around ignition. A rather uncommon pathway of producing electronically excited states of N_2 and O_2, without any plasma, leads to the production of $O(^1D)$. The dissociation of NH_3 into NH_2, NH and N by the plasma and combustion chemistry result in increased production of N radicals, by the reaction - $NH + NH_2 \rightarrow N + NH_3$, following which a unique set of three-body plasma reactions of the type $N + N + M \rightarrow N_2(a^1\Delta_g) + M$, obtained from Zhong et al. [33], produce almost all the available $N_2(a^1\Delta_g)$. Next, an electronic exchange reaction of $N_2(a^1\Delta_g)$, $N_2(a^1\Delta_g) + O_2 \rightarrow O_2(b^1\Delta_g) + N_2$ produces $O_2(b^1\Delta_g)$, which eventually reacts with the O radicals in the mixture, to form $O(^1D)$ by $O_2(b^1\Delta_g) + O \rightarrow O_2 + O(^1D)$.

Thus, the enhancement in OH production bolstered by the activated plasma chemistry (producing $O(^1D)$) is found to be responsible for the higher reactivity of CP1 (nanosecond plasma), as compared to CP6 (nanosecond thermal) and CP7 (continuous thermal) cases.

3.2. NO_x emission

The deleterious impact of NO_x emission (mainly NO and NO_2) on human health and the environment are well known [44–46], resulting in premature deaths and ozone depletion in upper atmosphere. Hence, NO_x emission of a potential fuel is one of the most important metrics to assess its viability to become a well-accepted fuel for combustion engines. Since ammonia is plagued with higher NO_x emission in comparison to traditional hydrocarbon-based fuels, evaluating whether non-equilibrium plasma can somehow help to reduce NO_x is a critical next step after assessing its benefits in terms of faster ignition. This section presents a parametric evaluation on the effects of plasma on NO_x emission from combustion of NH_3. The reduced electric field (E/N), equivalence ratio, pressure, and effect of nanosecond plasma are chosen as the major parameters to study the NO_x production. The effect of pulse energy and pulse frequency are not discussed in detail, as the observations are found to be rather straightforward: On increasing the pulse energy, a faster rise in temperature (see Fig. F.1 in supplementary materials) was found to effect a faster rise in NO, whereas, increasing the frequency only changed the time scale of NO production and final NO was found to be the same regardless of frequency.

It should be noted that due to the lack of concrete experimental NO_x measurements of plasma assisted ammonia combustion in canonical configurations such as homogeneous batch reactors, perfectly stirred reactors, etc., it is difficult to ascertain the uncertainty associated with the results presented in this section. Nonetheless, since the plasma chemistry mechanism is assembled using reactions from credible sources (mentioned in supplementary materials) and a well-validated combustion mechanism [20] is used, the trends predicted should at least be qualitatively correct. Moreover, the NO_x predictions in this paper do not directly translate to IC engine / gas turbine NO_x emissions, since the nanosecond glow / spark discharges in such combustion systems are only present in a very small region, which ignites the mixture and produces a flame kernel, that eventually leads to NO_x emissions. Nevertheless, the fundamental chemical kinetics for homogeneous, premixed mixtures of NH_3 in air discussed in this section will remain the same in the discharge region. Hence, it is worthwhile to understand the effect of plasma on NO_x production there.

3.2.1. Effect of reduced electric field (E/N)

Figure 19 show the NO and NO_2 number densities for cases CV1 (E/N = 150 Td) and CV4 (E/N = 550 Td). The number densities of NO and NO_2 remain almost equal during the plasma pulses, indicating negligible dependence of NO_x on the reduced electric field (E/N). Nevertheless, the higher rate of increase in temperature towards the end of pulses for CV1 compared to CV4 (see Fig. 5(a)) increases the thermal NO_x production for CV1, thereby depicting a slightly higher peak in the production of NO and NO_2 as seen in Fig. 19. This higher rate of rise in temperature during CV1 is found to be a consequence of the heat liberated by the VT relaxation reactions involving the vibrational states of NH_3 and N_2, as was discussed in Section 3.1.1.

3.2.2. Effect of equivalence ratio

Thermal NO_x (i.e., oxides of nitrogen formed due to reaction of nitrogen with oxygen in air at elevated temperatures) [47] is a predominant issue for the combustion of every fuel, when air is used as the oxidizer. High temperature and lean mixtures drive up the rates of thermal NO_x production reactions due to the excess oxygen content in lean mixtures and due to the exponential increase of rate constants with the increased temperature. The trend remains similar with plasma as well (see Fig. 20(a)), except that the

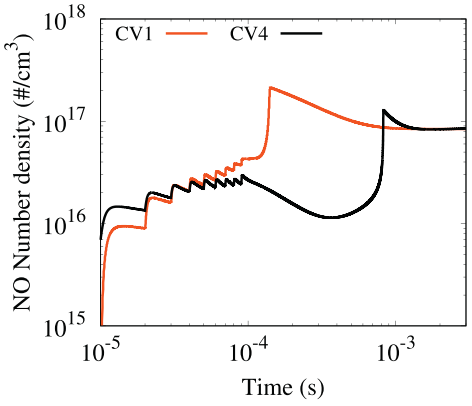

(a) NO Number density

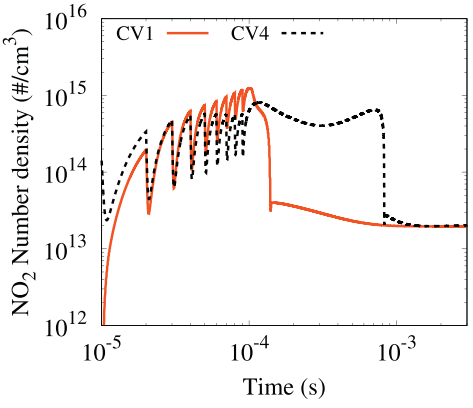

(b) NO_2 Number density

Fig. 19. Number densities of (a) NO and (b) NO_2 at reduced electric fields (E/N) of 150 Td (CV1, solid red lines) and 550 Td (CV4, dashed black lines) in a constant volume 0D reactor.

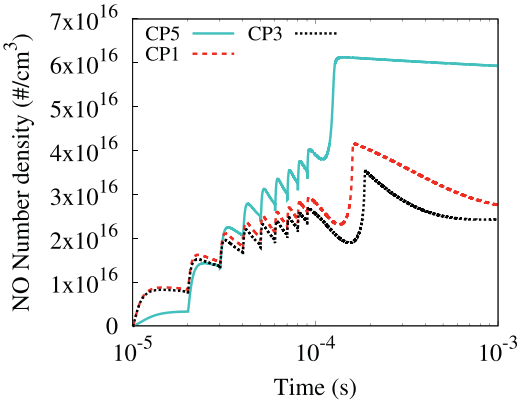

(a) NO Number density

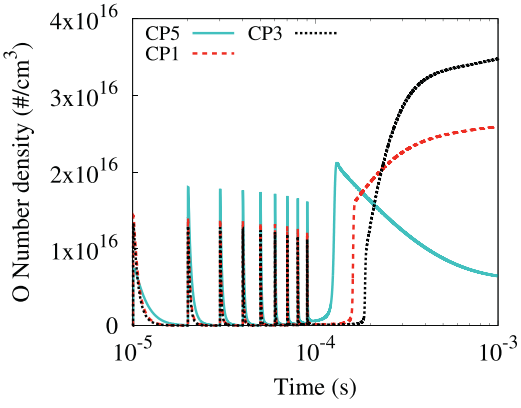

(b) O Number density

Fig. 20. Number densities of (a) NO and (b) O at $\phi = 0.5$ (CP5, solid cyan lines), $\phi = 1.0$ (CP1, dashed red lines), and $\phi = 1.2$ (CP3, dotted black lines), in a constant pressure 0D reactor. (For interpretation of the references to color in this figure legend, the reader is referred to the web version of this article.)

reactions contributing to NO production during the pulses are different. O radicals are mainly produced by electron impact reactions of O_2 and the subsequent reactions of O with the electronically excited states of N_2 to form NO during the pulses (see Fig. 21). The percentages of the quenching of the electronically excited states (i.e., $N_2(A)$, N_2(B), $N_2(C)$ and $N_2(a')$) remains almost the same for the lean (CP5), stoichiometric (CP1) and rich (CP3) cases as shown in Fig. 21. However, from Fig. 20(b), it can be seen that the peak O radical number density during the pulses reduces with increasing ϕ, which can be ascribed to the reduction of O_2 as ϕ increases. Thus, the curtailed production of O (during the pulses) with higher equivalence ratios explain the reduced production of NO_x (during pulses) with increasing ϕ as depicted in Fig. 20(a).

Also, the amount of NO during and post ignition is observed to be the least for CP3 (rich) and CP1 (stoichiometric) when compared to CP5 (lean) (see Fig. 20(a)). To understand the lower NO during and post-ignition, for the stoichiometric (CP1) and rich mixtures (CP3), the pathways consuming NO are probed into. At the instance of maximum NO number density after ignition, i.e. when NO consumption surpasses its production, significant differences were observed in the consumption pathways of NO for the rich (CP3) and stoichiometric (CP1) vs lean cases (CP5), as is shown in Fig. 22 (a) and (b). The relatively larger quantities of NH_2 and NH in cases CP3 and CP1 as compared to CP5 reduce NO to N_2 and NNH, thereby curbing the NO production after ignition. The lower number densities of these important radicals in CP5 yields very different pathways (Fig. 22 (b)) that are not very effective in consuming NO. Specifically, the NO reduction pathways of $NH_2 + NO \rightarrow NNH + OH$ and $NH_2 + NO \rightarrow N_2 + H_2O$ are in line with the hypothesis of Choe et al. [15] and the observations of traditional (non-plasma assisted) NH_3 combustion in Hayakawa et al. [5]. A further reduction in NO number densities are observed for cases CP1 and CP3 post ignition, when the NO number density gradually reduces towards it equilibrium value ($\sim$ 0.3 ms). This can be attributed to important NO de-oxygenation and NO reduction pathways, which are $N + NO \rightarrow N_2 + O$, $H_2 + NO \rightarrow H + HNO$ and $H_2 + NO \rightarrow NH + OH$. These pathways are dominant for CP1 (41%, 22% and 13% of NO consumption respectively) and CP3 (36%, 28% and 12% of NO consumption respectively). On the other hand, in CP5, the major pathways to consume NO post ignition are $NO + O + M \rightarrow NO_2 + M$, $H + NO + M \rightarrow HNO + M$ and $N + NO \rightarrow N_2 + O$ contributing to 52%, 29% and 5% of NO consumption. Moreover, post-ignition, the net NO consumption rates are as follows: 3 moles/m^3s (CP5 - lean) < 50 moles/m^3s (CP1 - stoichiometric) < 62 moles/m^3s (CP3 - rich) further justifying the slopes of the NO number density profiles in Fig. 20 (a). Increased availability of N radicals (two orders of magnitude higher for CP3 as compared to CP1) due to the plasma dissociation reactions, especially for the rich and stoichiometric cases as compared to the lean case, due to higher proportion of NH_3, and the high levels of NO reached during ignition, drive the major NO consumption reaction $N + NO \rightarrow N_2 + O$ in the forward direction. The reverse reaction is one of the three thermal NO_x formation reactions which is highly

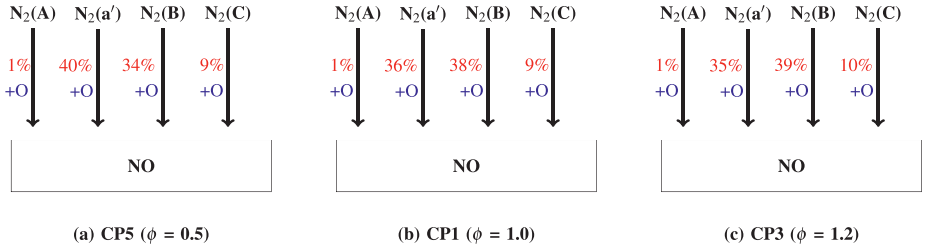

(a) CP5 (ϕ = 0.5) (b) CP1 (ϕ = 1.0) (c) CP3 (ϕ = 1.2)

Fig. 21. Production pathways of NO at (a) $\phi = 0.5$ (CP5), (b) $\phi = 1.0$ (CP1), and (c) $\phi = 1.2$ (CP3) during the last pulse in a constant pressure 0D reactor. The flux percentages are calculated relative to the produced NO species.

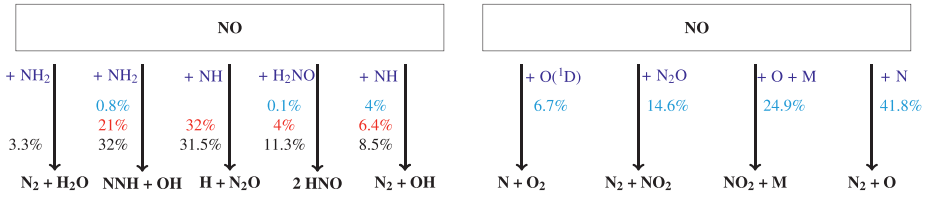

(a) Consumption pathways of NO for CP5, CP1, and CP3 (b) Major NO consumption pathways for CP5

Fig. 22. Consumption pathways of NO for $\phi = 0.5$ (CP5), $\phi = 1.0$ (CP1), and $\phi = 1.2$ (CP3) at the point of maximum NO number density (when NO consumption rates surpasses its production rate). The flux percentages represent NO consumption.

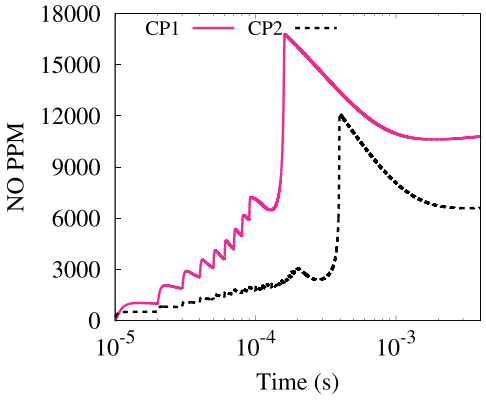

(a) NO Mole fraction

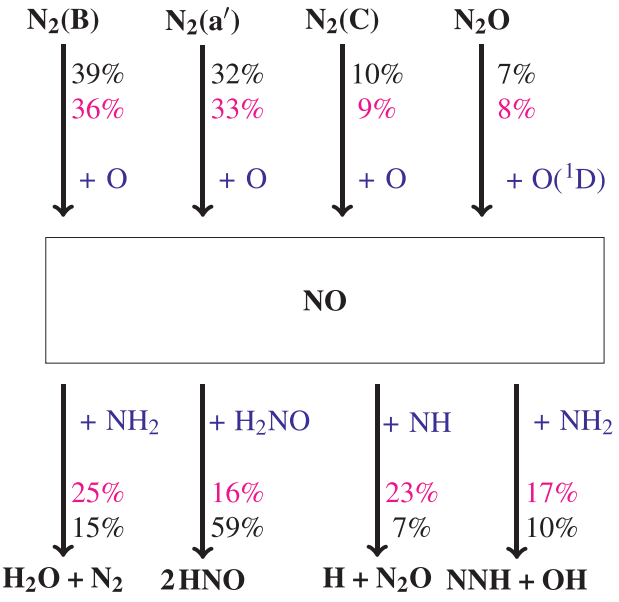

(b) NO production pathways

Fig. 23. (a) The mole fractions of NO and (b) the production and consumption path flux analysis of NO during and after the third pulse, at pressures of 1 atm (CP1, solid pink lines) and 3 atm (CP2, dashed black lines) in a constant pressure 0D reactor. The percentage colors correspond to that of the lines for CP1 and CP2.

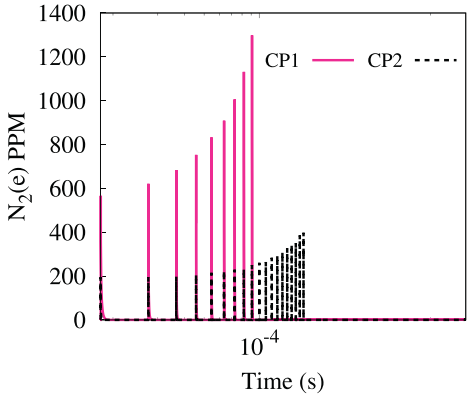

(a) N_2(e) Mole fraction - linear scale

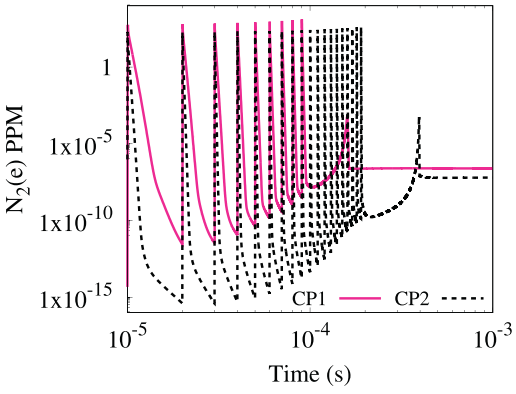

(b) N_2(e) Mole fraction - logarithmic scale

Fig. 24. Mole fractions (in PPM) of total electronic states of N_2 species (N_2(e)) plotted using a (a) linear scale and (b) logarithmic scale at pressures of 1 atm (CP1, solid pink line) and 3 atm (CP2, dashed black line) in a constant pressure 0D reactor.

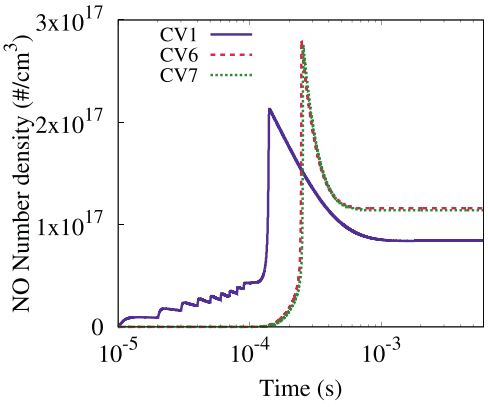

(a) NO

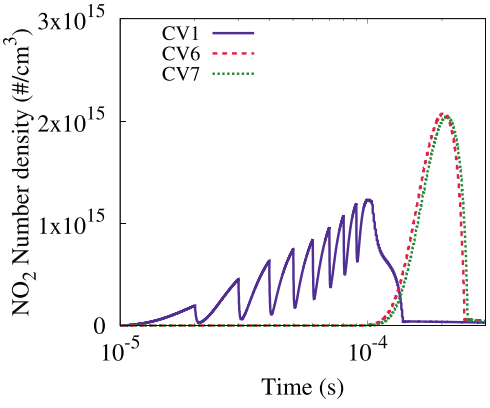

(b) NO_2

Fig. 25. Number densities of (a) NO and (b) NO_2 for nanosecond plasma energy deposition (CV1, solid indigo lines), nanosecond thermal energy deposition (CV6, dashed red lines), and continuous thermal energy deposition (CV7, dotted green lines) in a constant volume 0D reactor. (For interpretation of the references to color in this figure legend, the reader is referred to the web version of this article.)

endothermic as it requires breaking the N_2 triple bond. In traditional hydrocarbon combustion, the reverse reaction is known to be favored due to the limited availability of N radicals and the relatively lower values of NO produced during ignition.

3.2.3. *Effect of pressure*

The effect of pressure on the production of NO is discussed in this section. Since the case CP2 (3 atm constant pressure) has 3x increased densities of NH_3, N_2 and O_2 to begin with as compared to the case CP1 (1 atm constant pressure), this section utilizes the species mole fractions instead of number densities to compare the NO emission between CP1 and CP2.

Figure 23 (a) shows the NO profiles for CP1 (1 atm) and CP2 (3 atm). At the end of the plasma pulses, the NO mole fraction for CP1 is observed to be about ~4,000 PPM higher than that of CP2. Moreover, this difference in NO between CP1 and CP2 is found to be almost the same post-ignition (~4,000 PPM), indicating similar rise in NO levels for CP1 and CP2 during ignition. This was observed despite depositing twice the total energy in case CP2 (20 pulses) for it to successfully ignite. Thus, the overall higher NO in case of CP1 can be attributed to the enhanced production of NO by plasma chemistry at lower pressures. To ascertain the role of plasma chemistry in the production of NO, a production and consumption flux analysis for NO has been performed during the third pulse ($\sim 2\times10^{-5}$ s) and during the inter-pulse gap between the third and fourth pulses respectively, for both CP1 and CP2, and is shown in Fig. 23(b). It can be observed that almost all of the NO (for both CP1 and CP2) is produced by the reactions $N_2(e) + O \rightarrow NO + N(^2D)$ and $N_2O + O(^1D) \rightarrow NO + NO$, where, $N_2(e)$ represents the electronically excited states of N_2 ($N_2(a')$, N_2(B), and $N_2(C)$). These electronically excited species are produced by the electron-impact reaction $E + N_2 \rightarrow E + N_2(e)$ and $E + O_2 \rightarrow E + O(^1D) + O$. From Fig. 23 $N_2 \rightarrow N_2(e) \rightarrow NO$ is the major channel of NO production.

Figure 24 (a) and (b) depicts the mole fraction of all electronically excited states of N_2 (represented by N_2(e)) both using a linear and logarithmic scale on the y-axis. The linearly scaled plot shows the overall higher mole fraction of N_2(e) during the pulses for CP1 (1 atm). And the logarithmic scaled plot shows the difference in both overall mole fractions and the rates of quenching of N_2(e) during the inter-pulse gaps. Clearly, the higher rate of quenching of the electronically excited states of N_2 at higher pressures (CP2) result in a mole fraction that is almost 4–5 orders of magnitude lower than those at lower pressures (CP1). It should also be noted that the quantity of N_2(e) produced during the pulses is actually higher for CP2, but since they get quenched to a much greater extent during the inter-pulse gaps, the overall mole fractions of N_2(e) are higher for CP1. This is because higher pressure increases the number of collisions, resulting in higher rates of electron impact reactions during the pulse as well as quenching reactions of excited states and ions during the gaps. Similar explanation holds

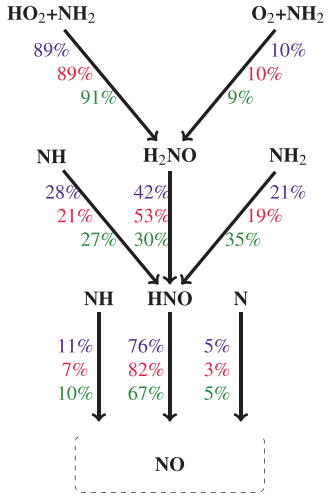

Fig. 26. Production pathways of NO during ignition for nanosecond plasma energy deposition (CV1, indigo), nanosecond thermal energy deposition (CV6, red), and continuous thermal energy deposition (CV7, green) in a constant volume 0D reactor. The flux percentages are calculated relative to the produced species and the colors used for flux percentages are in accordance with Fig. 25. (For interpretation of the references to color in this figure legend, the reader is referred to the web version of this article.)

for the production and consumption of $O(^1D)$ as well. Hence, even though the major pathways for the production and consumption of these excited states remain the same, the rates of these pathways are faster for CP2 as compared to CP1 (overall consumption rates of $O(^1D)$, $N_2(B)$ and $N_2(a')$ are 1mole/m^{3}s, 25 moles/m^{3}s and 5 moles/m^{3}s for CP1 as compared to 5mole/m^{3}s, 69 moles/m^{3}s and 23 moles/m^{3}s for CP2, respectively. These values are obtained at a certain point during the inter-pulse where their respective densities are reduced by an order of magnitude as compared to the maximum value produced during the pulse. However, the overall trend of faster quenching remains applicable during the first 100–500 nanoseconds of the inter-pulse gaps, where these excited states are expected to quench the fastest.)

3.2.4. Effect of nanosecond pulsed non-equilibrium plasma

When non-equilibrium plasma was used (CV1), peak NO and NO_2 number densities are reduced by almost 25% and 75% immediately after ignition, and the final post-ignition NO and NO_2 number densities are reduced by approximately 33% as compared to the nanosecond thermal (CV6) and continuous thermal (CV7) discharges, as shown in Fig. 25. It is worth noting that case CV1 produces the highest NO_x during the plasma pulses, but least levels after ignition. However, in combustion systems such as gas turbines and internal combustion engines, it makes sense to compare the NO_x production after the ignition process. Thus, to understand the reduced NO_x production in CV1 immediately after ignition, path flux analyses have been performed to compare the production pathways of NO in cases of CV1, CV6, and CV7 at the instance of ignition.

Figure 26 shows the path flux analysis for the production of NO for CV1 (nanosecond plasma), CV6 (nanosecond thermal), and CV7 (continuous thermal). The analysis points out the major pathway in the production of NO to be $NH_2 \rightarrow H_2NO \rightarrow HNO \rightarrow NO$, indicating the importance of NH_2 radicals for the production of NO at the instance of ignition. Figure 27 shows the number densities of NH_3 and NH_2 for the cases CV1, CV6 and CV7. Figure 27(a) portrays a quicker consumption of NH_3 during the pulses of CV1 ($\sim$ 25% drop), and Fig. 27(b) shows a higher production of NH_2 during pulses of CV1, when compared to CV6 and CV7. To unravel the effect of this increased consumption of NH_3 (or alternatively,

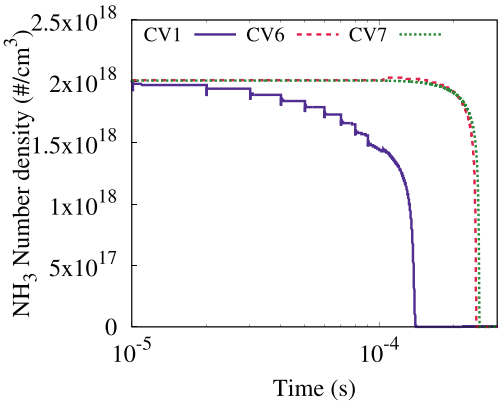

(a) NH3

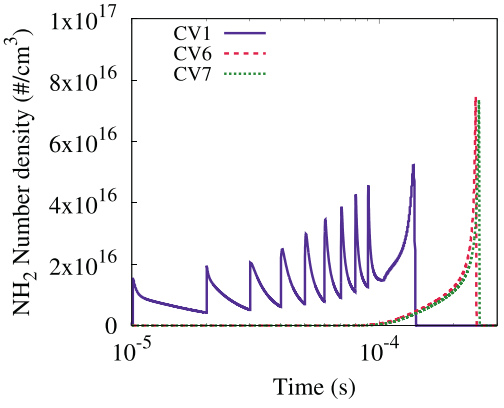

(b) NH_2

Fig. 27. Number densities of (a) NH_3 and (b) NH_2 for nanosecond plasma energy deposition (CV1, solid indigo lines), nanosecond thermal energy deposition (CV6, dashed red lines), and continuous thermal energy deposition (CV7, dotted green lines) in a constant volume 0D reactor. (For interpretation of the references to color in this figure legend, the reader is referred to the web version of this article.)

the increased production of NH_2) during the plasma discharge on the production of NO immediately after ignition, path flux analyses are performed to understand the consumption of NH_3 during the plasma discharge and ignition and are presented in Fig. 28.

During the plasma discharge (CV1), the NH_2 radicals produced from NH_3 is predominantly consumed to form N_2 through $NH_2 \rightarrow NH \rightarrow N \rightarrow N_2$, $NH_2 \rightarrow N_2$, and $NH_2 \rightarrow NNH \rightarrow N_2$ (see Fig. 28(a)). This reforming of NH_3 by plasma at low temperatures reduces the amount of NH_3 available at the instance of ignition, as depicted by Fig. 27(a). However,in the absence of plasma discharge (CV6), almost all of the initial NH_3 is available at ignition. The NH_3 available at the instance of ignition mostly ends up producing NH_2, NH, and N (see Fig. 28(b)). Unlike the consumption of NH_2, NH, and N to mostly produce N_2 during plasma, a significant portion of these species are converted to various oxygenated species (NO, NO_2, and HNO) during ignition as seen in Fig. 28(b). Since the plasma reforms about 25% of NH_3 to N_2, lesser NH_3 is available during the ignition to produce NO in the case of CV1 when compared to CV6. It is interesting to note that radicals such as NH and NH_2 can help in reducing NO after ignition, when the NO consumption rate surpasses the NO production rate (as was discussed in Section 3.2.2), but can also aid in increasing NO production at the instance of ignition, as is the case for thermal ignition.

In summary, the reforming of NH_3 to produce N_2 during the plasma pulses in CV1 results in the decreased production of NO

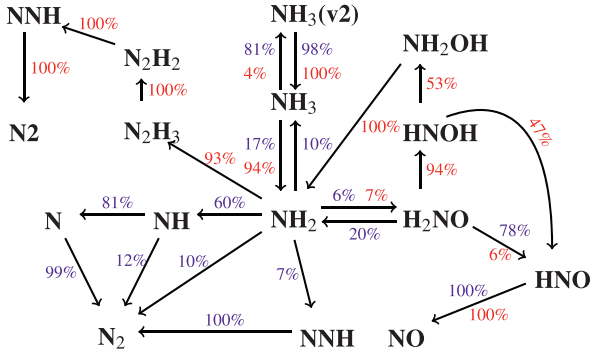

(a) NH_3 consumption during plasma

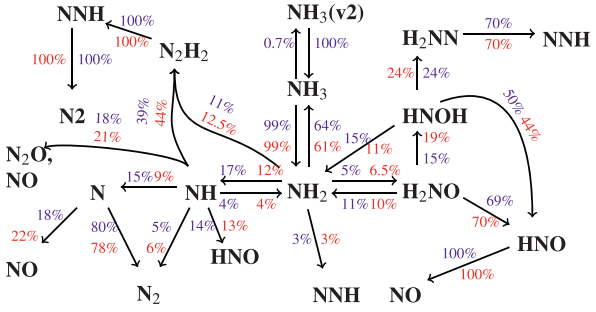

(b) NH_3 consumption at ignition

Fig. 28. Consumption pathways of NH_3 during (a) the 5th pulse and (b) at ignition for nanosecond plasma energy deposition (CV1) and nanosecond thermal energy deposition (CV6) in a constant volume 0D reactor. The flux percentages are calculated relative to the consumed species and the color used for flux percentages is in accordance with Fig. 25.

post-ignition. For the cases of CV6 and CV7, almost all of the initial NH_3 is available at the instance of ignition, thereby leading to increased production of NO immediately post-ignition through various pathways. It is also evident that NO produced during the pulses in typically formed due to excitation and quenching reactions of N_2 and O_2 in the air, facilitated by the plasma. On the other hand, plasma pulses also help to reform NH_3 to N_2 to eventually limit the fuel-bound NO_x - a pathway that is missing in the thermal energy deposition case. After all the NH_3 is consumed, the overall NO levels are determined by the thermal NO_x pathways that produce higher NO for CV6 / CV7 (thermal ignition) than CV1, simply due to the higher final temperatures (CV1: 2890 K, CV6 / CV7: 3030 K)

4. Conclusion

Computational analysis of constant volume and constant pressure ignition of ammonia-air mixtures using non-equilibrium plasma discharges have been performed. Ignition delay and NO_x emission were chosen as the targets to assess the feasibility of considering NH_3 as a mainstream fuel for internal combustion engines and gas turbines. Reduced electric field (E/N), equivalence ratio, pulse frequency, energy density per pulse and pressure were chosen as the controllable parameters whose impact have been both qualitatively and quantitatively determined. Moreover, the role of non-equilibrium plasma chemistry to promote fast ignition and lower the post-ignition NO_x levels have been emphasized by comparing it against equivalent nanosecond thermal and continuous thermal discharge cases. The salient findings of the present study are outlined as below:

- While energy density per pulse and pulse frequency had a fairly proportionate and expected impact on the ignition delay, more probing was required to understand the dependence on the other parameters.
- Given the higher electron energy loss fraction towards vibrational excitation at lower reduced electric fields (represented by a value of 150 Td in this work), vibrational-to-translational (VT) relaxation associated with N_2 was observed to be a predominant factor in the decrease of ignition delay at lower reduced electric fields. Nevertheless, no significant effect was found in the production of NO_x due to VT relaxation.
- Lean mixtures were found to ignite faster owing to the lower rate of consumption of OH radicals via $NH_3 + OH \rightarrow NH_2 + H_2O$ between pulses, compared to the stoichiometric and rich mixtures. However, lean mixtures produce higher NO than stoichiometric and rich mixtures during the plasma discharge, primarily due to the presence of excess O radicals produced by the plasma on account of the higher O_2 content in lean mixtures. At the point of maximum NO number densities, just after ignition, fuel radicals such as NH_2 and NH were found to help in NO reduction for the rich and stoichiometric mixtures. The drop in post-ignition NO for stoichiometric and rich mixtures is attributed to the de-oxygenation and reduction of NO through pathways $NO + N \rightarrow N_2 + O$, $H_2 + NO \rightarrow H + HNO$ and $H_2 + NO \rightarrow NH + OH$.
- Within the pressure range of this study (i.e., 1–3 atm), at the higher pressure (i.e., 3 atm), the ignition delay was found to increase due to the reactivity-inhibiting pressure dependent recombination reaction producing HO_2 ($H + O_2 + M \rightarrow HO_2 + M$). Moreover, higher pressures resulted in lower production of NO, but produced higher levels of NO_2 due to the pressure dependent recombination reaction producing N_2H_4, and subsequently producing H_2NN followed by NO_2. Nevertheless, the total NO_x was found to reduce at higher pressures, primarily due to increased rates of collisional quenching reactions of the electronically excited states of N_2 and O_2 during the inter-pulse gaps.
- Most importantly, the incorporation of non-equilibrium plasma discharges were found to reduce the ignition delay as a consequence of the plasma kinetics producing significant reactive OH radicals. Non-equilibrium plasma was also found to reduce the production of NO_x, on account of the faster consumption of NH_3 to produce N_2 during plasma discharges, thereby limiting the availability of NH_3 and NH_2 radicals at ignition to produce NO_x.

To summarize, the activation of plasma kinetics significantly improves the reactivity of NH_3/air mixtures along with the convenience of lesser NO_x production, thus suggesting the advantages in incorporating plasma assisted ammonia combustion systems in real-world engines. However, it should be noted that while plasma can help in abating NO production, premixed ammonia combustion in air still produces a lot more NO than what is acceptable of real-world engines, and thus, further upstream / downstream NO reduction or reforming techniques (plasma or non-plasma based) could be helpful to adopt NH_3 as a carbon-free fuel alternative for power generation and transportation.

Declaration of Competing Interest

The authors declare that they have no known competing financial interests or personal relationships that could have appeared to influence the work reported in this paper.

Acknowledgments

S. Yang acknowledges the faculty start-up funding from the University of Minnesota and the grant support from NSF CBET 2002635. T.S. Taneja acknowledges the support from the UMII MnDRIVE Graduate Assistantship Award. The authors acknowledge the fruitful discussions with Dr. Xingqian Mao, Dr. Yuan Wang, Dr. Timothy Y. Chen, Prof. Joseph K. Lefkowitz and Ms. Galia Faingold during the development of the 0D solver and for inputs on compiling the plasma mechanism for ammonia. The authors also acknowledge the Minnesota Supercomputing Institute (MSI) for the computational resources.

Supplementary material

Supplementary material associated with this article can be found, in the online version, at doi:10.1016/j.combustflame.2022.112327

References

[1] H. Kobayashi, A. Hayakawa, K.D.K.A. Somarathne, E.C. Okafor, Science and technology of ammonia combustion, Proc. Combust. Inst. 37 (2019) 109–133.
[2] S. Wiseman, M. Rieth, A. Gruber, J.R. Dawson, J.H. Chen, A comparison of the blow-out behavior of turbulent premixed ammonia/hydrogen/nitrogen–air and methane–air flames, Proc. Combust. Inst. 38 (2021) 2869–2876.
[3] C. Lhuillier, P. Brequigny, F. Contino, C. Mounaïm-Rousselle, Experimental study on ammonia/hydrogen/air combustion in spark ignition engine conditions, Fuel 269 (2020) 117448.
[4] A. Valera-Medina, M. Gutesa, H. Xiao, D. Pugh, A. Giles, B. Goktepe, R. Marsh, P. Bowen, Premixed ammonia/hydrogen swirl combustion under rich fuel conditions for gas turbines operation, Int. J. Hydrogen Energy 44 (2019) 8615–8626.
[5] A. Hayakawa, T. Goto, R. Mimoto, T. Kudo, H. Kobayashi, NO formation/reduction mechanisms of ammonia/air premixed flames at various equivalence ratios and pressures, Mech. Eng. J. (2015) 14–00402.
[6] A.P.E. York, Ammonia as hydrogen carrier for transportation; investigation of the ammonia exhaust gas fuel reforming 5, Int. J. Hydrogen Energy 38 (2013) e9917.
[7] Y. Yu, Y.-M. Gan, C. Huang, Z.-H. Lu, X. Wang, R. Zhang, G. Feng, Ni/La_2O_3 and Ni/MgO–La_2O_3 catalysts for the decomposition of NH_3 into hydrogen, Int. J. Hydrogen Energy 45 (2020) 16528–16539.
[8] A. Klerke, C.H. Christensen, J.K. Nørskov, T. Vegge, Ammonia for hydrogen storage: challenges and opportunities, J. Mater. Chem. 18 (2008) 2304–2310.
[9] G. Faingold, J.K. Lefkowitz, A numerical investigation of NH_3/O_2/He ignition limits in a non-thermal plasma, Proc. Combust. Inst. 38 (2021) 6661–6669.
[10] X. Mao, A. Rousso, Q. Chen, Y. Ju, Numerical modeling of ignition enhancement of CH_4/O_2/He mixtures using a hybrid repetitive nanosecond and DC discharge, Proc. Combust. Inst. 37 (2019) 5545–5552.
[11] J.K. Lefkowitz, P. Guo, A. Rousso, Y. Ju, Low temperature oxidation of methane in a nanosecond pulsed plasma discharge, 53rd AIAA Aerospace Sciences Meeting (2015), p. 0665.
[12] A. Rousso, S. Yang, J. Lefkowitz, W. Sun, Y. Ju, Low temperature oxidation and pyrolysis of n-heptane in nanosecond-pulsed plasma discharges, Proc. Combust. Inst. 36 (2017) 4105–4112.
[13] Y. Zhang, S. Yang, W. Sun, V. Yang, Effects of non-equilibrium plasma discharge on ignition and NTC chemistry of DME/O_2/Ar mixtures: a numerical investigation, 53rd AIAA/SAE/ASEE Joint Propulsion Conference (2017), p. 4773.
[14] A. Shioyoke, J. Hayashi, R. Murai, N. Nakatsuka, F. Akamatsu, Numerical investigation on effects of nonequilibrium plasma on laminar burning velocity of ammonia flame, Energy Fuel 32 (2018) 3824–3832.
[15] J. Choe, W. Sun, T. Ombrello, C. Carter, Plasma assisted ammonia combustion: simultaneous NO_x reduction and flame enhancement, Combust. Flame 228 (2021) 430–432.
[16] L. Dai, S. Gersen, P. Glarborg, H. Levinsky, A. Mokhov, Experimental and numerical analysis of the autoignition behavior of NH_3 and NH_3/H_2 mixtures at high pressure, Combust. Flame 215 (2020) 134–144.
[17] X. Han, Z. Wang, Y. He, Y. Liu, Y. Zhu, A.A. Konnov, The temperature dependence of the laminar burning velocity and superadiabatic flame temperature phenomenon for NH_3/air flames, Combust. Flame 217 (2020) 314–320.
[18] J. Otomo, M. Koshi, T. Mitsumori, H. Iwasaki, K. Yamada, Chemical kinetic modeling of ammonia oxidation with improved reaction mechanism for ammonia/air and ammonia/hydrogen/air combustion, Int. J. Hydrogen Energy 43 (2018) 3004–3014.
[19] P. Glarborg, J.A. Miller, B. Ruscic, S.J. Klippenstein, Modeling nitrogen chemistry in combustion, Prog. Energy Combust. 67 (2018) 31–68.
[20] B. Mei, X. Zhang, S. Ma, M. Cui, H. Guo, Z. Cao, Y. Li, Experimental and kinetic modeling investigation on the laminar flame propagation of ammonia under oxygen enrichment and elevated pressure conditions, Combust. Flame 210 (2019) 236–246.
[21] E.C. Okafor, Y. Naito, S. Colson, A. Ichikawa, T. Kudo, A. Hayakawa, H. Kobayashi, Experimental and numerical study of the laminar burning velocity of CH_4–NH_3–air premixed flames, Combust. Flame 187 (2018) 185–198.
[22] K.P. Shrestha, L. Seidel, T. Zeuch, F. Mauss, Detailed kinetic mechanism for the oxidation of ammonia including the formation and reduction of nitrogen oxides, Energy Fuel 32 (2018) 10202–10217.
[23] X. Mao, Q. Chen, A.C. Rousso, T.Y. Chen, Y. Ju, Effects of controlled non-equilibrium excitation on H_2/O_2/He ignition using a hybrid repetitive nanosecond and DC discharge, Combust. Flame 206 (2019) 522–535.
[24] S. Nagaraja, V. Yang, Z. Yin, I. Adamovich, Ignition of hydrogen–air mixtures using pulsed nanosecond dielectric barrier plasma discharges in plane-to-plane geometry, Combust. Flame 161 (2014) 1026–1037.
[25] S. Pancheshnyi, B. Eismann, G. Hagelaar, L.C. Pitchford, Computer Code ZDPlasKin, University of Toulouse, Laplace, Technical Report, CNRS-UPS-INP, Toulouse, France www. zdplaskin. laplace. univ-tlse. fr, 2008.
[26] R.J. Kee, F.M. Rupley, E. Meeks, J.A. Miller, CHEMKIN-III: a FORTRAN Chemical Kinetics Package for the Analysis of Gas-Phase Chemical and Plasma Kinetics, Technical Report, Sandia National Labs., Livermore, CA (United States), 1996.
[27] J.K. Lefkowitz, P. Guo, A. Rousso, Y. Ju, Species and temperature measurements of methane oxidation in a nanosecond repetitively pulsed discharge, Philos. Trans. R. Soc. A 373 (2015) 20140333.
[28] T.S. Taneja, S. Yang, Numerical modeling of plasma assisted pyrolysis and combustion of ammonia, AIAA Scitech 2021 Forum (2021), p. 1972.
[29] G. Hagelaar, L.C. Pitchford, Solving the Boltzmann equation to obtain electron transport coefficients and rate coefficients for fluid models, Plasma Sources Sci. T. 14 (2005) 722.
[30] P.N. Brown, A.C. Hindmarch, G.D. Byrne, Dvode, computer subroutine package for solving ordinary differential equations,(August 31, 1992) (1992).
[31] F. Tholin, A. Bourdon, Simulation of the hydrodynamic expansion following a nanosecond pulsed spark discharge in air at atmospheric pressure, J. Phys. D Appl. Phys. 46 (2013) 365205.
[32] D.L. Rusterholtz, D.A. Lacoste, G.D. Stancu, D.Z. Pai, C.O. Laux, Ultrafast heating and oxygen dissociation in atmospheric pressure air by nanosecond repetitively pulsed discharges, J. Phys. D Appl. Phys. 46 (2013) 464010.
[33] H. Zhong, C. Yan, C.C. Teng, T.Y. Chen, G. Wysocki, Y. Ju, Kinetic studies of excited singlet oxygen atom O(^{1}D) reactions with ethanol, Int. J. Chem. Kinet. 53 (6) (2021) 688–701.
[34] H. Zhong, C. Yan, C.C. Teng, T. Chen, A.C. Rousso, G. Wysocki, Y. Ju, Kinetic studies of excited singlet oxygen atoms O(^{1}D) reactions with fuels in plasma assisted combustion, AIAA Scitech 2019 Forum (2019), p. 2065.
[35] S. Yang, S. Nagaraja, W. Sun, V. Yang, Multiscale modeling and general theory of non-equilibrium plasma-assisted ignition and combustion, J. Phys. D Appl. Phys. 50 (2017) 433001.
[36] S. Pancheshnyi, S. Biagi, M.C. Bordage, G. Hagelaar, W.L. Morgan, A.V. Phelps, L.C. Pitchford, The LXCat project: electron scattering cross sections and swarm parameters for low temperature plasma modeling, Chem. Phys. 398 (2012) 148–153.
[37] Hayashi database, 1987, (www.lxcat.net).
[38] M. Hayashi, Personal communication to the JILA Atomic Collisions Data Center, 1987.
[39] J.W. Dreyer, D. Perner, C.R. Roy, Rate constants for the quenching of N_2 ($A^3\Sigma_u^+$, $v_A = 0–8$) by CO, CO_2, NH_3, NO, and O_2, J. Chem. Phys. 61 (1974) 3164–3169.
[40] F.E. Hovis, C.B. Moore, Vibrational relaxation of $NH_3(\nu_2)$, J. Chem. Phys. 69 (1978) 4947–4950.
[41] J. Hong, S. Pancheshnyi, E. Tam, J.J. Lowke, S. Prawer, A.B. Murphy, Kinetic modelling of NH_3 production in N_2–H_2 non-equilibrium atmospheric-pressure plasma catalysis, J. Phys. D Appl. Phys. 50 (2017) 154005.
[42] P. Sabia, M.V. Manna, A. Cavaliere, R. Ragucci, M. de Joannon, Ammonia oxidation features in a jet stirred flow reactor. the role of NH2 chemistry, Fuel 276 (2020) 118054.
[43] D.G. Goodwin, R.L. Speth, H.K. Moffat, B.W. Weber, Cantera: an object-oriented software toolkit for chemical kinetics, thermodynamics, and transport processes, 2021, (https://www.cantera.org). Version 2.5.1. 10.5281/zenodo.4527812
[44] W.B. Innes, Effect of nitrogen oxide emissions on ozone levels in metropolitan regions, Environ. Sci. Technol. 15 (1981) 904–912.
[45] C.J. Weschler, H.C. Shields, D.V. Naik, Indoor chemistry involving O_3, NO, and NO_2 as evidenced by 14 months of measurements at a site in Southern California, Environ. Sci. Technol. 28 (1994) 2120–2132.
[46] J.E. Jonson, J. Borken-Kleefeld, D. Simpson, A. Nyíri, M. Posch, C. Heyes, Impact of excess NO_x emissions from diesel cars on air quality, public health and eutrophication in europe, Environ. Res. Lett. 12 (2017) 094017.
[47] C.T. Bowman, Kinetics of pollutant formation and destruction in combustion, Prog. Energy Combust. 1 (1975) 33–45.